Journal of Geodynamics 122 (2018) 25–40

Contents lists available at ScienceDirect

Journal of Geodynamics

journal homepage: www.elsevier.com/locate/jog

Invited Research Article

Bayesian surface reconstruction of geodetic uplift rates: Mapping the global fingerprint of Glacial Isostatic Adjustment

Laurent Husson[a,*], Thomas Bodin[b], Giorgio Spada[c], Gaël Choblet[d], Corné Kreemer[e]

[a] Université Grenoble Alpes, CNRS, ISTerre, Grenoble, France
[b] Univ Lyon, Université Lyon 1, Ens de Lyon, CNRS, Lyon, France
[c] Dipartimento di Scienze Pure e Applicate, Urbino University, Urbino, Italy
[d] Université de Nantes, CNRS, Laboratoire de Planétologie et Géodynamique, Nantes, France
[e] Nevada Bureau of Mines and Geology, Nevada Seismological Laboratory, University of Reno, NV, USA

ARTICLE INFO

Keywords:
GPS
Vertical land motion
GIA

ABSTRACT

We use a global compilation of geodetic (GPS) rates to reconstruct vertical land motion (VLM) using a Bayesian inference method. Trends of VLM are derived from almost 15,000 GPS position time-series retrieved from the Nevada Geodetic Laboratory. Our *Transdimensional Regression* (TR) method is based on Voronoi tessellation and self-adapts to the level of spatial structure contained in the database. It is thus suitable for our strongly heterogeneous dataset, both in terms of the geographical distribution and level of uncertainties, and provides at each location a probability density function for the rate of VLM. We apply the TR method to a set of globally distributed regions. At high latitudes the signal is dominated by Glacial Isostatic Adjustment (GIA); fast uplift rates are observed across the previously ice-covered areas, while subsidence characterizes the surrounding peripheral forebulges. Other long-wavelengths processes, like dynamic topography, occasionally overprint and out-pace the GIA signal. Short-wavelength processes can be disentangled; remarkable examples are the sharp boundary between the uplifting Himalaya and subsiding foreland Ganges plain, the fast subsiding Central Valley of California, or the subsiding Galveston area (Texas) and Mississippi delta. In an attempt to visualize the global signature of GIA, we assembled the regional maps and filtered out the short-wavelength components. Comparison to independent models (dynamic model predictions of GIA) or data (relative sea level change along coastlines) reveals that our map of VLM is robust and dominated by GIA. Conversely, in regions where TR predictions are robust, departure between the two classes of models (dynamic predictions and TR) either reveals that other processes than GIA may locally contribute to the signal, or to incorrect model predictions. For example, on the edges of formerly ice-covered regions, TR predicts larger negative gradients of uplift rates than dynamical models, most probably due to the poor knowledge of the effective rheological structure of the Earth that alters the predictions of dynamic GIA models.

1. Introduction

Vertical land motion (VLM) occurs globally in response to a variety of processes, ranging from long-term geodynamic processes to anthropogenic activity (e.g. Pfeffer et al., 2017). Amongst those, *Glacial Isostatic Adjustment (GIA)* is probably the most significant and obvious global cause of VLM. At a global scale and at discernible rates, it only competes with tides on a short time scale (daily to annual), and mantle convection on a longer time scale. GIA rates up to several millimetres per year are expected in deglaciated regions but the GIA contribution can be of the order of 1 mm/yr also in far field regions (e.g. Spada, 2017). Together with the current absolute sea-level rise of anthropogenic origin, GIA is contributing to the current variations of relative sea-level along the world's coastlines, which are of concern for policy makers (e.g. Tamisiea, 2011; Kopp et al., 2016; Spada, 2017). At present-day, GIA is dominantly affected by the deglaciation that occurred from the *Last Glacial Maximum* (*LGM*, at ~20 ka) until the Holocene maximum (at ~6 ka). This is exemplified by the emblematic uplift of several hundreds of meters beneath the former continental ice sheets, where the associated post-glacial rebound is still occurring at several mm/yr (e.g. Ekman, 1996; Steffen et al., 2009; Kierulf et al., 2014; Simon et al., 2017). Importantly, the effects of GIA are not limited to the regions covered by thick ice sheets at the LGM. In fact, regional and local isostatic disequilibrium following the latest

* Corresponding author.
E-mail address: laurent.husson@univ-grenoble-alpes.fr (L. Husson).

https://doi.org/10.1016/j.jog.2018.10.002
Received 23 May 2018; Received in revised form 12 September 2018; Accepted 19 October 2018
Available online 31 October 2018

deglaciation are still causing variations of relative and absolute sea level, gravity field variations, and horizontal and vertical movements of the solid Earth, at all latitudes (Wu and Peltier, 1982). Since the work of Farrell and Clark (1976), models of GIA bloomed (see the reviews of Whitehouse, 2009, 2018). GIA models essentially stem from a description of the history of melting of the continental ice sheets (e.g. Lambeck et al., 2003, 2014; Peltier et al., 2015), a realistic model for the Earth's rheology field, and a *Sea Level Equation* (SLE Farrell and Clark, 1976), which describes the response of a spherically layered viscoelastic Earth model to surface loading (e.g. Spada, 2017). Most GIA models assume a spherically symmetrical Earth and a linear Maxwell viscoelastic rheology (Spada et al., 2011). Ignoring lateral variations in mantle rheology, as well as non-linear rheological effects (Sabadini and Gasperini, 1989; Giunchi et al., 1997; Austermann et al., 2013) is likely to bias the predictions of GIA models, possibly affecting the accuracy of present-day surface velocity predictions. A usual assumption in GIA modeling, i.e. that the time evolution of the ice sheets is not coupled to sea level variations, is a further limitation (Whitehouse, 2018).

As an alternative to modeling, direct geodetic observations can be employed to quantify GIA. This is routinely done regionally (e.g. Bouin and Wöppelmann, 2010), but can also be done globally. The surface of the Earth is constantly monitored, with an improving resolution, using a range of techniques. To quantify VLM, the long tide gauge records, which monitor the deformation of both the surface of the oceans and of the solid Earth, can be useful (e.g. Choblet et al., 2014). In order to extract the sole contribution from the solid Earth, and ultimately that of the GIA, some knowledge on the contribution from the oceans is required, which can be gained from satellite altimetry (e.g. Ostanciaux et al., 2011; Pfeffer and Allemand, 2016; Pfeffer et al., 2017). Last, direct observations of VLM are available from a variety of geodetic sensors (*GNSS* – Global Navigation Satellite System, *VLBI* – Very Long Baseline Interferometry, *SLR* – Satellite Laser Ranging, etc.) but only GNSS products provide a sufficient geographic coverage to appraise VLM. They have been extensively used for horizontal deformation (Kreemer et al., 2014), and more recently for VLM (Hammond et al., 2016; Santamaría-Gómez et al., 2017). The recent *MIDAS* (Median Interannual Difference Adjusted for Skewness) compilation of trends of VLM by the Nevada Geodetic Laboratory (NGL), derived from GPS time series, provides an unprecedented opportunity to infer VLM at a global scale (Blewitt et al., 2018). The large dataset produced by MIDAS represents an ensemble of linear trends associated to given GPS stations. These observations are therefore discrete, unevenly distributed spatially, and bear variable levels of uncertainties. In addition, the relevance of an independent and localized measurement of vertical rate, as an indicator of large-scale geodynamic processes like GIA, is often uncertain. Interpolating individual data partly overcomes this issue by taking advantage of the neighboring data points. In this way, the part of the signal that is due to local effects, or not spatially coherent, is considered as data noise.

Reconstructing a 2D continuous surface from a discrete set of local observations is a recurring problem in Earth sciences and geostatistics. Most surface fitting algorithms used estimate surface values from weighted averages of nearby data points, a procedure justified by the assumption that the surface varies smoothly with distance. For example, kriging (e.g. Stein, 1999) assumes that the statistics (e.g. the covariance) of the field to be recovered are spatially invariant. This assumption is clearly violated in our case, as tectonically active regions may show higher spatial variation in vertical rates compared to more stable regions where the long-wavelength contribution of GIA dominates. Weighted-average schemes differ in how they assign weights to the constraining values. The simplest methods assign a polynomial or power law weight dependence as a function of distance. Another commonly used approach is to fit a 2D cubic spline function where the smoothness of the function is determined by a tension parameter (Smith and Wessel, 1990). A well known limitation of these methods is that the solution strongly depends on choices made by the user at the outset (e.g. level of smoothness). Imposing an arbitrary level of smoothness biases the solution in a statistical sense, and does not allow to properly propagate data uncertainties toward confidence limits in the surface (Aster et al., 2005).

Here we propose to address these issues with a Bayesian surface reconstruction algorithm (Bodin et al., 2012; Choblet et al., 2014) to reconstruct probabilistic 2D maps of VLM. Our regression scheme accounts for spatially heterogeneous data statistics, does not require any user-defined smoothing parameter, and is able to provide uncertainties in the reconstructed surface. The objective is therefore to provide a critical assessment of VLM as revealed by a large ensemble of GPS measurements over a large region, as opposed to robust but sparser assessments of individual measurements (e.g. Pfeffer et al., 2017). We first illustrate the TR method by comparing it to two different methods (GPS Imaging, Hammond et al., 2016, and linear regression with splines), recently applied in two different regions (California/Nevada and Western Alps/Italy, respectively). We then expand our analysis to a series of regional maps that encompass the entire world. The resulting merged global map is then filtered and analyzed in search of the GIA fingerprint. That map is made available and can be used as an alternative to forward model predictions of GIA. Last, the two regions where the signal is most documented, namely Europe and North America, are analyzed at a higher resolution, and compared to estimates of relative sea level change along the coastlines.

2. Bayesian surface reconstruction of vertical land motion from GPS data

2.1. Time series and MIDAS processing

The NGL makes GPS time-series from permanent GPS (cGPS, *continuous* GPS) stations routinely available, together with a rate estimated using the *MIDAS* (Median Interannual Difference Adjusted for Skewness) (Blewitt et al., 2016) algorithm. As of December 2017, NGL presents rates for 14,663 stations worldwide (Fig. 1). MIDAS computes, on each individual time-series, the median of the trends obtained between two points separated by approximately one year. As a result, MIDAS estimated rates are not affected by seasonality and discontinuities, regardless of their origins, and thus gives robust long-term rates of VLM, except where there is significant post-seismic deformation (Hammond et al., 2016). MIDAS also provides a realistic estimate of trend uncertainty that we use in the following as a measure of the local uncertainty. The data are released in the global reference frame given by the International GNSS Service 2008 (IGS08, the IGS realization of ITRF2008, Rebischung et al., 2012, referenced to the center of mass).

Uplift rates in the MIDAS database are approximately symmetrically disposed about zero, with a median value of -0.11 mm/yr (Fig. 2a). The standard deviation of the vertical velocities around the inverted trend increases with the rates. This is illustrated by the variation of the median value (1000 data bins) of the standard deviation as a function of the absolute trend of VLM (Fig. 2b). A latitudinal dependence of the uplift rates is apparent (Fig. 2c), with higher rates at high latitudes: median and mean values at high latitudes – higher than 55°N and lower than 55°S – are 3.0 and 4.0 mm/yr, respectively. This pattern manifests, to first order, the effects of GIA. Last, for a variety of technical reasons, sampling from the GPS devices themselves occasionally fails. For a given station, the total number of recovered daily records actually used by MIDAS is therefore lower than or equal to the total number of days of activity (Fig. 2c). Median (1000 data bins) recovery has a mean value of 78% and it almost systematically exceeds 70%; it degrades from 100% for the shortest time series to 70% for the longest time series.

Prior to inverting the data, we preliminary discard uncertain trends from the entire database. First, we arbitrarily filter out trends obtained from time series with a span of less than 2 years or with cumulated record lengths lower than 10% of the total duration of the record.

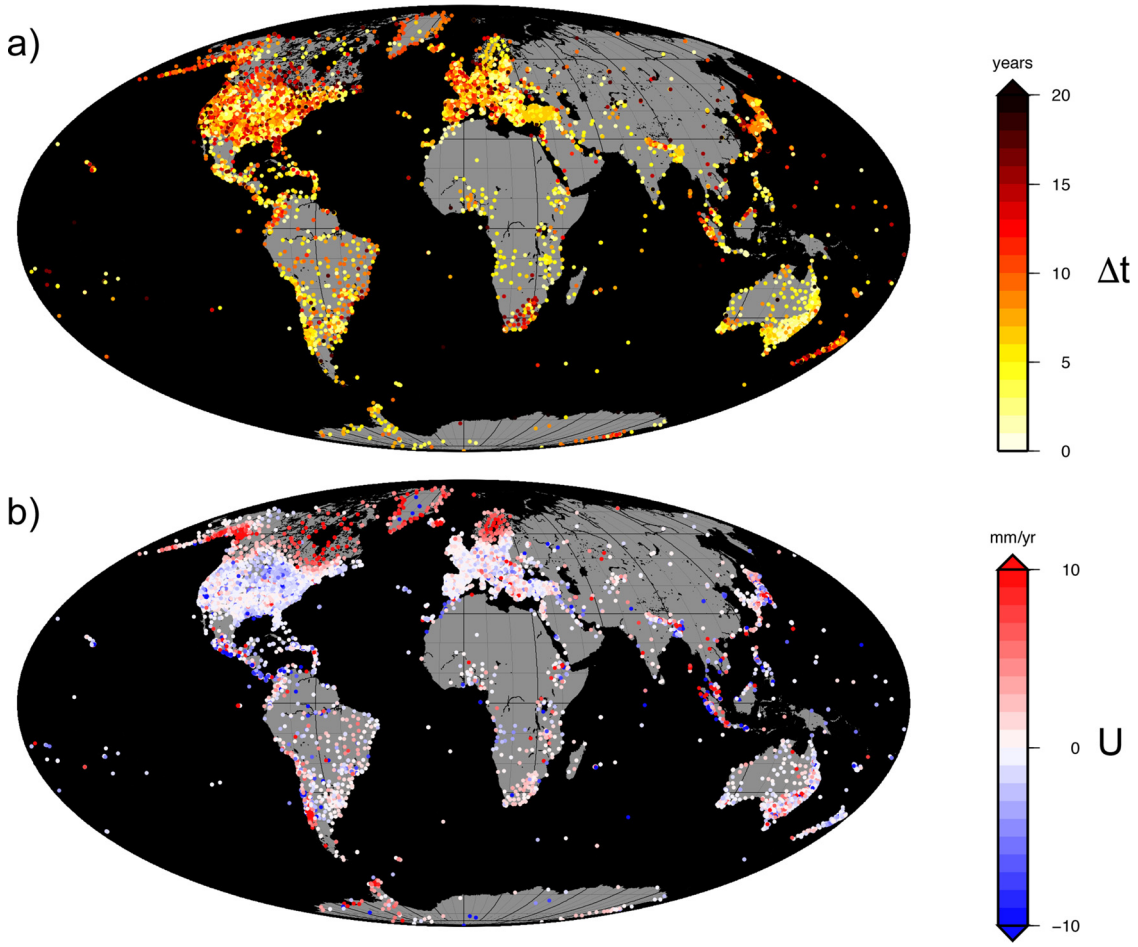

Fig. 1. World view of MIDAS database (as of December 2017), color coded as a function of duration of the time series Δt (a), and local uplift rate U (b).

Although some of these short series may formally show low uncertainties, they cannot cautiously be taken into consideration. We additionally exclude trends exceeding 30 mm/yr in amplitude, since this is the maximum expected rate in regions subject to fast deglaciation like Patagonia (Dietrich et al., 2010), Alaska (Freymueller et al., 2013) or Greenland (Spada et al., 2012). This selection is highly permissive, but is only meant to exclude data that shall not be considered as reliable, regardless of their apparent uncertainties. We additionally exclude time series that have a standard deviation higher than 2 mm/yr. Again, since GIA models predict VLM at rates lower than 2 mm/yr except at high latitudes (e.g. Spada et al., 2011; Geruo et al., 2013; Argus et al., 2014), this threshold is loose and is meant to remove time series characterized by a suspect temporal variability, which probably would demand a (manual) careful examination. We also exclude trends from stations located on ice (AMU2 AMUN GLS1 GLS2 GLS3 LTHW REC1 REC2 SMM1 SMM2 SUMM UTHW), as well as station GIL1 (North America), which is located near a dam in the Nelson river, and stations D198 and D219 in Germany, that were erroneously archived at the time of processing. Given all these conditions, we consider 10,602 trends. The rates in the residual dataset (Fig. 2c) have a median value of −0.12 mm/yr (mean is very close to 0 mm/yr), and a standard deviation of 2.7 mm/yr, the large value of which reflecting the weight of the data at high latitudes.

2.2. Transdimensional regression

At a global scale, a straightforward interpolation in principle requires a uniform distribution of data points, but also a uniform distribution of data quality. These requirements are, not surprisingly, violated by the database (Fig. 1). First, oceans are almost entirely deprived of data points; second, the density of data points greatly varies across continental domains. In some regions – Europe and North America in particular – the density is more than ten times higher than in other places as Africa, South America, Antarctica, or Asia. In addition, the data quality is spatially heterogeneous. Most important is the duration of the record (Fig. 1a), which further penalizes regions where systematic GPS monitoring has only happened relatively recently. Finally, the temporal continuity of the record can be critical too. We therefore expect the level of structure (smoothness) as well as the level of uncertainty in the recovered 2D surface to be highly heterogeneous.

In general, 2D regression schemes require that the reconstructed surface fits the data in a least squares sense, while minimizing some global metric (e.g., level of smoothness, spline tension, distance to a reference surface). Standard algorithms often involve a few tunable parameters, which results in two well-known problems. First, the level of smoothness is usually spatially uniform across the surface, which prevents the solution from accounting for the uneven spatial distribution of information. Second, the arbitrary choice for tuning parameters -needed to prevent extreme values in the surface and to ensure spatial continuity of the solution- bias the solution in a statistical sense and does not allow proper propagation of data uncertainties toward confidence limits in the surface.

Here we propose to address these issues by formulating our 2D regression problem as a Bayesian inverse problem, where the solution is defined as the probability of a surface given the set of local observations. We approximate this distribution with a transdimensional regression (TR) algorithm as described in Bodin et al. (2012) and Choblet et al. (2014). The surface is parameterized on a Cartesian grid with an

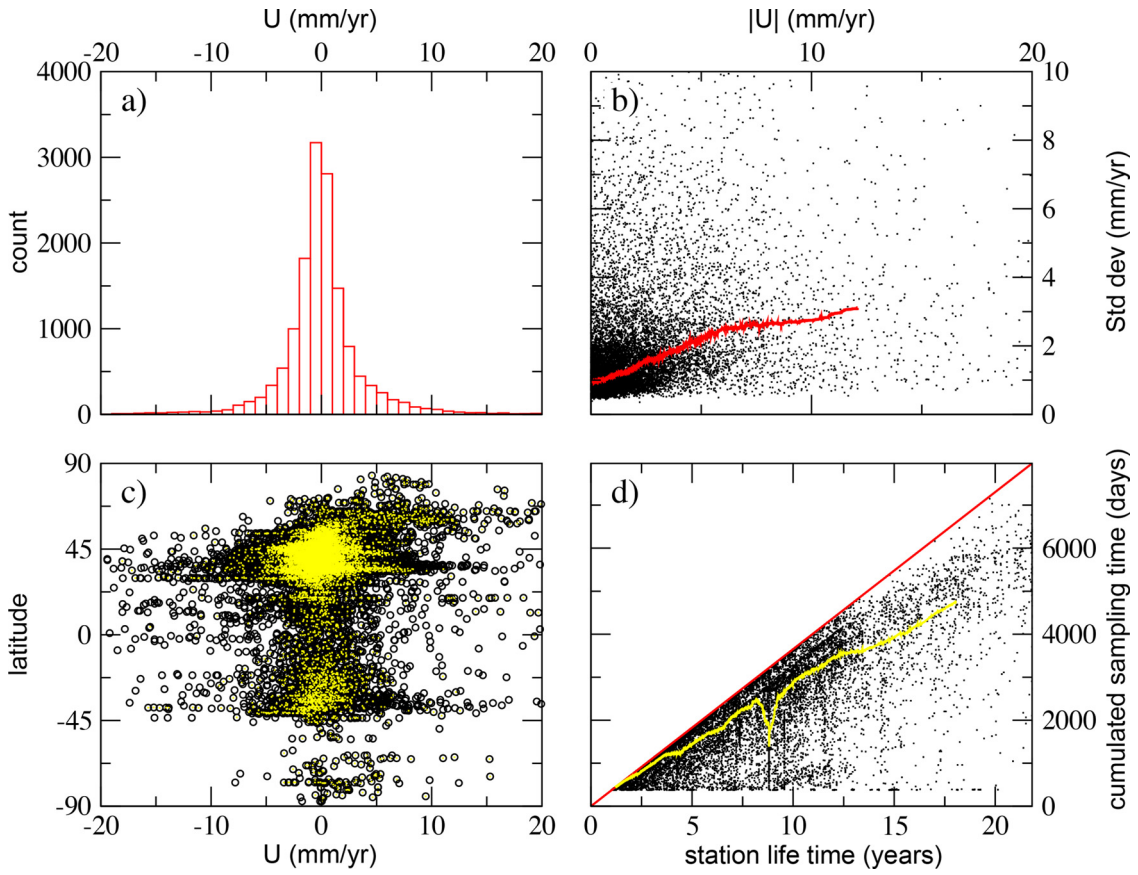

Fig. 2. MIDAS database, as of December 2017. (a) Histogram of vertical motion rate U; (b) standard deviation (ordinates) and absolute vertical motion rate $|U|$ (abscissae). Red curve is the median (1000 data bins); (c) latitudinal dependency of the vertical motion rate U, all data (black circles), selected data (yellow crosses), see text for a description of the selection criteria applied; (d) cumulated sampling time as a function of station life time; red line shows a 100% sampling rate; yellow curve shows the median recovery (1000 data bins).

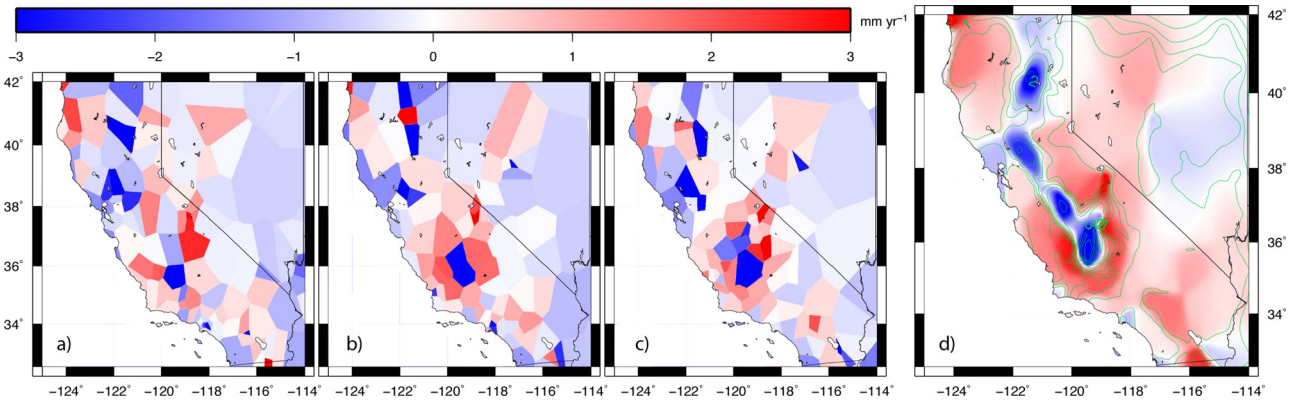

Fig. 3. Vertical land motion in California, as inferred from GPS data (dataset from Hammond et al., 2016): Panels (a)–(c) show three examples of individual Voronoi tesselations. These models are distributed according to the target distribution that represents the probability of the unknown surface, given the data. Panel (d) shows the average value (color-coded) and the standard deviation (green curves, 0.5 mm/yr interval) over the large ensemble of models.

irregular mesh consisting of a variable number of Voronoi cells (Voronoi, 1908) as shown in Fig. 3. Since the number of nodes defining the surface is variable, the problem is known to be transdimensional, i.e., the dimension of the parameter space is itself variable (Green, 1995; Sambridge et al., 2012). Although Voronoi cells seem complex structures, the mesh is uniquely controlled by a small number of nodes, that are randomly perturbed at each step of the algorithm. A constant value of vertical rate is assigned to each Voronoi cell, yielding a surface made of piecewise uniform polygons. Note that the number and position of the nodes are variable and independent of the position of GPS stations. In this way, the parameterization of the surface will self-adapt to the data distribution.

We use the reversible jump Markov chain Monte Carlo (rj-McMC) algorithm to generate an ensemble of Voronoi models, for which the distribution approximates the probability of the unknown surface (Geyer and Møller, 1994; Green, 1995, 2003). The solution is represented by an ensemble of several thousands of Voronoi models with variable parameterizations. There are a number of ways to look at this ensemble of models. For example, at any geographical location, one can extract a number of statistical measures across the ensemble of models (mean, median, maximum, and standard deviation). Fig. 3 shows results for California, where the maps on the right represent the mean and

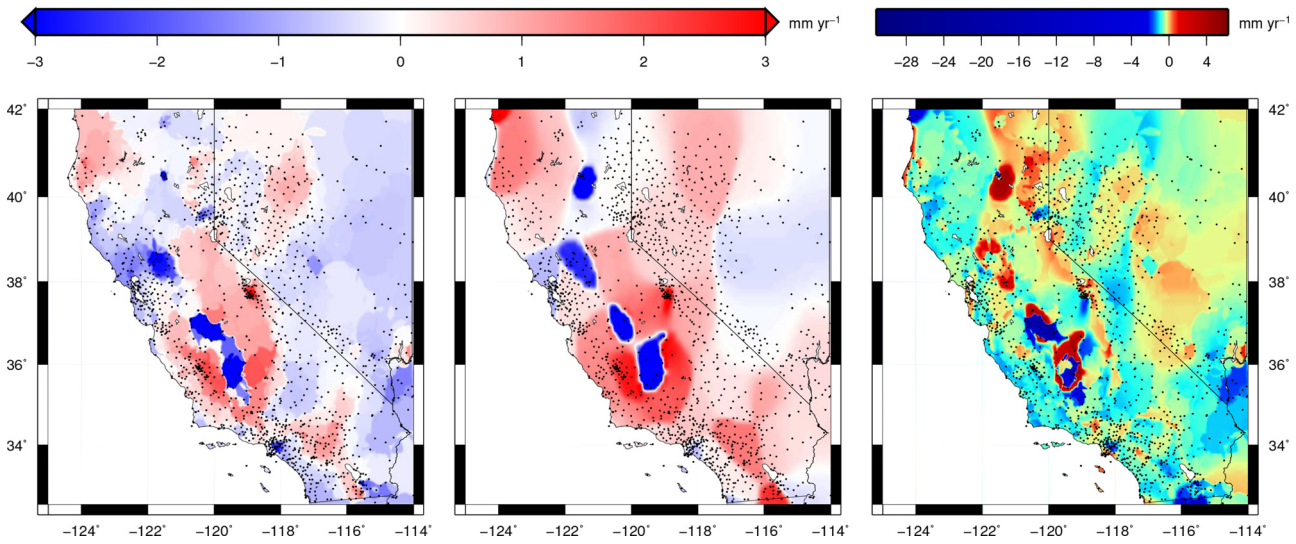

Fig. 4. GPS inverted vertical land motion across California and Nevada. (a) Median rate obtained from *GPS Imaging* (Hammond et al., 2016). (b) Median rate of the posterior distribution, current study (TR). (c) Difference between the two. Black dots represent GPS stations. Positive (negative) values show uplift (subsidence). Models inverted from MIDAS database, as of May 2016; NA12 reference frame (as in Hammond et al., 2016).

standard deviation of the probabilistic surface at each location.

Transdimensional regression accounts for uncertainties that are propagated from the data to the uncertainties in the inferred surface. The MIDAS compilation delivers a trend for each station, but also an estimate of its variability and temporal segmentation of the record. We take advantage of these metrics in our inversion. We use a hierarchical formulation where the absolute level of error in the data becomes an unknown to be inverted for (Malinverno and Briggs, 2004; Malinverno and Parker, 2006; Dettmer et al., 2012). We set the level of error associated to each individual station as proportional to the value given by the MIDAS database, with the constant of proportionality σ being the parameter to invert for. This unknown scaling factor σ is constant over the entire dataset. That is, we use the information about relative data uncertainties given by the MIDAS database, and invert for the absolute level of errors (see Bodin et al., 2012, for details).

The Bayesian formulation requires to define an *a priori* probability distribution for unknown parameters, i.e. a range of values that are acceptable for these parameters. For the recovered surface, we define a maximum and minimum value of vertical rates. We adjust this range depending on the region of interest, from a joint inspection of three datasets: (i) dynamic model predictions of GIA; (ii) the result of a preliminary inversion which has a large range of admissibility, that we leave unchanged for all regions (± 25 mm/yr); (iii) the database itself, which involves a manual – and subjective – assessment of the a priori range of VLM. Details on the parametrization are given in Appendix, Table 1.

An important benefit of this method resides in the evaluation of the quality of the interpolation. This inversion procedure aims at globally yet critically assessing an irregular field of data, and shall not be confounded with the accurate evaluation of the robustness of individual records from local stations (as in, e.g. Bouin and Wöppelmann, 2010; Pfeffer and Allemand, 2016, for GPS and tide gauges). This inversion method was successfully applied to diverse fields of geosciences, for example reconstructing Moho depth from uneven estimates from seismology (Bodin et al., 2012), reconstructing relative sea level change from tide gauges (Choblet et al., 2014), or for river profiling geomorphology (Fox et al., 2015).

2.3. Regional case studies and comparisons: California/Nevada; Western Alps/Italy

Several studies compiled and interpolated VLM rates for chosen regions prior to the current study, using different methods. Relevant examples, where rates are high and show significant lateral contrasts are the California/Nevada region (Hammond et al., 2016) and the Western Alps and Italian peninsula (Serpelloni et al., 2013). While the first one opts for an elaborated interpolation method (referred to as *GPS Imaging*), the second uses the more straightforward *surface* spline interpolator of the Generic Mapping Tools (GMT) distribution (Wessel et al., 2013). Here, we take advantage of these substantially different approaches to appraise the added value of our method. The aim is not to benchmark the studies, for the *true* solution is unknown, but to compare the outcomes of each method. Because the two datasets of linear trends for these two regions have been measured with different schemes, uncertainties associated with these two datasets have been computed differently and have different level of amplitudes. The hierarchical Bayes approach allows us to treat the absolute level of uncertainties as unknown, and hence will account for these differences when fitting a surface.

First, MIDAS-derived VLM data were previously interpolated in the region covered by the states of Nevada and California, following the GPS Imaging procedure described in Hammond et al. (2016). We use the same input data, which are in the NA12 reference frame (Blewitt et al., 2013). Their hybrid method defines a *spatial structure function* which quantifies the level of "structure" between stations. This serves as a basis to compute weighted medians at each station which, in turn, are used to estimate median values at gridded evaluation points (Fig. 4a). This method succeeds in reproducing complex VLM fields and can account for discontinuities caused by faults; for example, the interpolated image sharply jumps from the Sierra Nevada, which uplifts at ~2 mm/yr, to the Central Valley, which subsides at rates exceeding ~ −2 mm/yr.

The transdimensional regression method that we propose here reveals comparable features (Fig. 4b). In particular, small scale structures are common outcomes of both methods, like the sharp transition between the uplifting Sierra Nevada and the subsiding Central Valley. Similarly, uplift is found to the west along the Coast Ranges, where the San Andreas Fault Zone resides. TR also shows regional responses and predicts a background structure, which uplifts at 1–2 mm/yr. To the east, in Nevada, this trend decreases and eventually turns into a slow rate of subsidence (< 0.5 mm/yr) to the east of the Central Nevada Seismic Belt, in the Basin and Range. However, major differences emerge when subtracting the median rates maps from one another (Fig. 4c). TR predicts an overall faster uplift of the entire region than

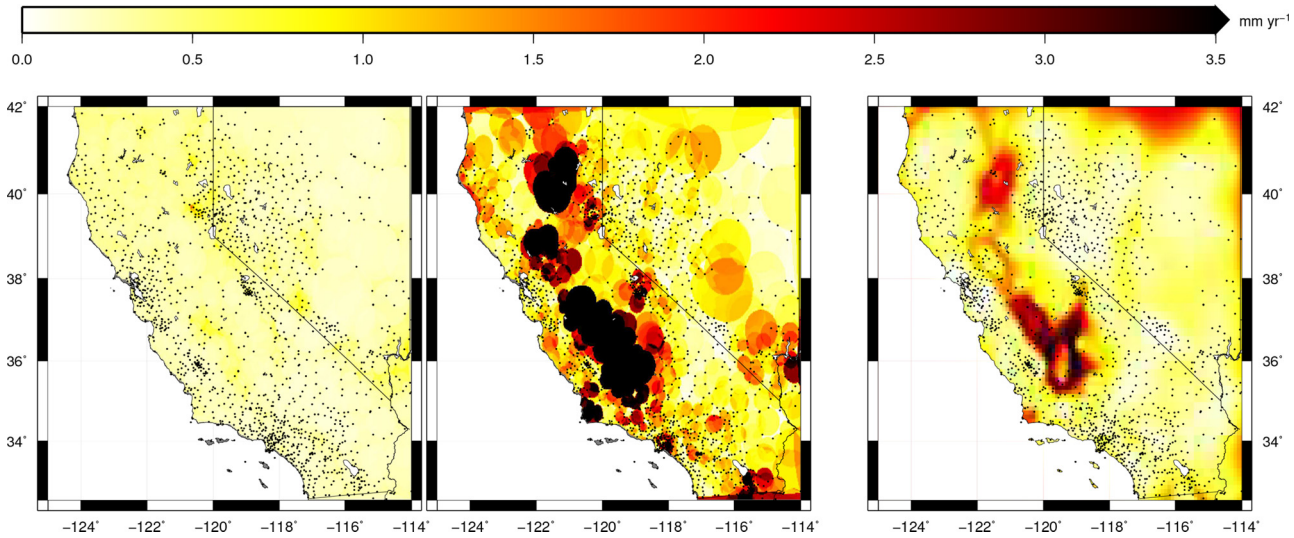

Fig. 5. Uncertainty in vertical land motion inverted from GPS data, California and Nevada. (a) Uncertainty in the weighted means of contributing rates (see details in Hammond et al., 2016). (b) Root-mean square residual scatter of contributing values (see Hammond et al., 2016). (c) Current study, Transdimensional Regression. Scale saturates at 3.5 mm/yr, covering 100% of the range in GPS Imaging a) and TR (c), and ~90% in GPS Imaging (b). Black dots represent GPS stations. Models inverted from MIDAS database, as of May 2016; NA12 reference frame (as in Hammond et al., 2016).

the GPS Imaging of Hammond et al. (2016). Small scale differences arise too; for example, to the north, the mountain range centered around Lassen Peak, around [−121.5°, 40.5°], is predicted to subside some 2 mm/yr faster with TR than GPS Imaging. The Central Valley of California is predicted to subside in a wider area with TR, but at a smaller rate at its center. This is graphically expressed (Fig. 4c) by the concentric uplift/subsidence patterns around [−120°, 36°]. Noteworthy, GPS Imaging-predicted subsidence in the Central Valley is extremely fast, with rates faster than −25 mm/yr in the Central Valley (Fig. 4a), whereas TR suggests subsidence rates of ~−4 mm/yr (Fig. 4b). TR treats uncertainties in the data as proportional to uncertainties provided by MIDAS, with the constant of proportionality σ defined as an unknown parameter to be inverted for. Here, the posterior distribution on σ is centered around 1, meaning that the level of fit obtained by our individual Voronoi models is comparable to the level of errors in the MIDAS dataset.

Thus to first order, the two techniques yield comparable trends and structures (Fig. 4a and b), but, apparently large discrepancies are striking too, which could suggest that results from the two methods depart and are irreconcilable (Fig. 5c). Mean rates (−0.24 mm/yr for GPS Imaging and 0.21 mm/yr for TR) and median rates (−0.22 mm/yr for GPS Imaging and 0.10 mm/yr for TR), for instance, readily attest for their mismatch. However, the differences between the two methods shall also be examined in the light of their uncertainties. Surface uncertainties from GPS Imaging are either expressed by the weighted mean rates (Fig. 5a) or on the basis of the residual scatter of GPS rates (Fig. 5b). The uncertainties so quantified vary dramatically, depending on the method employed, and can be thought of as lower and upper bounds, respectively. In the first case, modest uncertainties are obtained, with a median value of 0.25 mm/yr, a mean value of 0.27 mm/yr, and a standard deviation of 0.1 mm/yr. The second case is more severe: while the median uncertainty is only 0.87 mm/yr, the mean uncertainty is 3.21 mm/yr, and the standard deviation of the uncertainty amounts to ~10.0 mm/yr. Surface uncertainties from TR have a median value of 0.67 mm/yr, a mean of 1.17 mm/yr, and a standard deviation of ~1.0 mm/yr. Maximum uncertainties derived from the first method for GPS Imaging and for TR are 2.1 mm/yr and 3.5 mm/yr, respectively. For the second method for GPS Imaging, maximum uncertainty is as high as 87 mm/yr in the Central Valley, and 10% of the values are higher than 3.2 mm/yr. TR uncertainties are overall between the two extreme uncertainty estimates provided by GPS Imaging.

Regardless of the method employed, high uncertainties are found in areas where control points are relatively sparse and rates vary quickly laterally. Such regions, like the Central Valley, are also the places where the discrepancy is larger than the sum of uncertainties. Given the extremely high rates obtained with GPS Imaging, the associated uncertainties are more plausibly reflected by the high range estimate, *i.e.* the second method. Within such uncertainties, the GPS Imaging and TR methods overall agree. However, alternative methods – for instance based on joint GPS and InSAR data (Argus et al., 2017) – point to higher rates of subsidence than those obtained from TR. We interpret this discrepancy from two related aspects: the first one is that our method is conservative, and only reveals peak rates where they are fully supported by the data, most importantly considering the level of uncertainty attached to them. Given these constraints, or the lack thereof, the model avoids over-fitting observations. Secondly, some time series may not be easily modeled with a linear trend, because they critically respond to the highly variable demand on the aquifers over the time period (see e.g. Faunt and Sneed, 2015) and on the drought that affects the recharge of the aquifers and load on adjacent Sierra Nevada (see Amos et al., 2014; Argus et al., 2017). This causes strong temporal variations in VLM that considerably increase modeling uncertainties, and therefore, dampens the inverted subsidence rates in the Central Valley when using TR. This results does not mean that high subsidence rates are not present in the Central Valley, but point to the fact that complementary local observations of VLM – ideally obtained from independent methods – are needed to give a robust assessment.

However, alternative methods – for instance based on joint GPS and InSAR data (Argus et al., 2017) – point to higher rates of subsidence than those obtained from TR. We interpret this discrepancy to arise from two related aspects: the first one is that our method is conservative, and only reveals peak rates where they are fully supported by the data, most importantly considering the level of uncertainty attached to them. The second point is that we expect time series to be time-variable, because they critically respond to the highly variable demand on the aquifers over the time period (see e.g. Faunt and Sneed, 2015) and on the droughts that affect the recharge of the aquifers and variably loads the adjacent sierra Nevada (see Amos et al., 2014; Argus et al., 2017). This causes both spatial and temporal variations in VLM that considerably increase uncertainties, and therefore, dampens the inverted subsidence rates in the Central Valley wen using TR. This result does not mean that high subsidence rates are not present in the Central

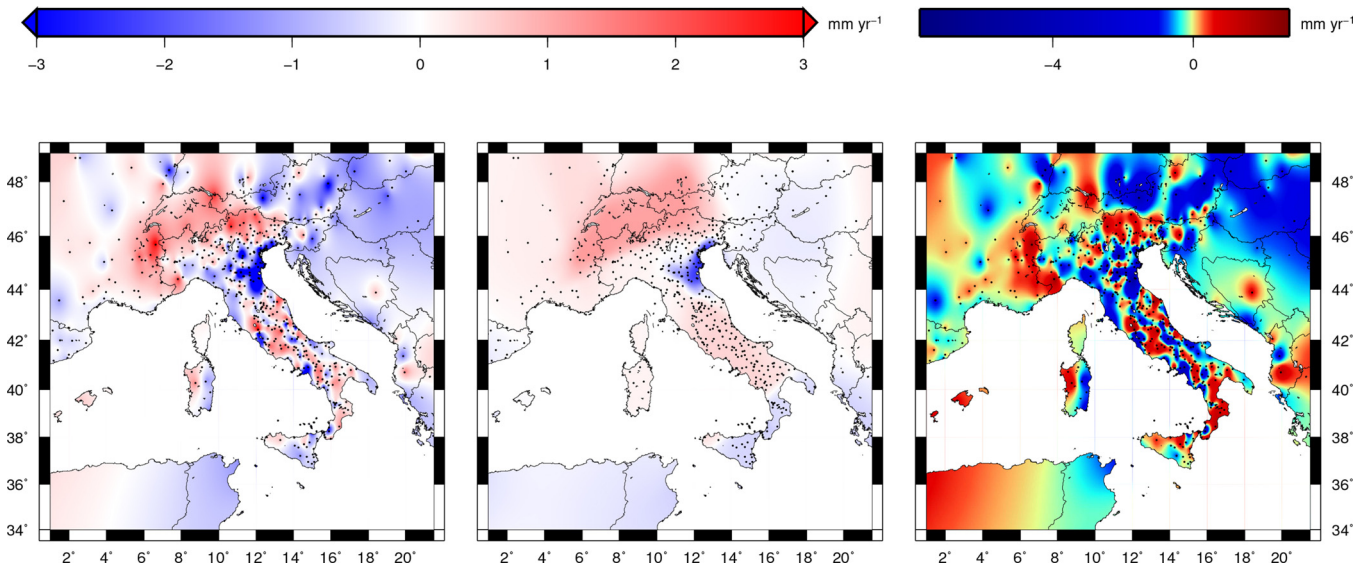

Fig. 6. Vertical land motion inverted from GPS data, Western Alps and Italy. (a) Mean rate derived from a spline interpolation (Serpelloni et al., 2013). (b) Mean rate of the posterior distribution, current study, Transdimensional Regression. (c) Difference between the two. Black dots represent GPS stations. Positive (negative) values show uplift (subsidence). Models inverted from GPS data compilation (provided by Serpelloni et al., 2013).

Valley, but points to the fact that more data – ideally obtained from independent methods – are needed to give a truly reliable assessment. We note that Hammond et al. (2016) are equally cautious when discussing the subsidence rates they obtain from GPS Imaging; They mention that the "strongest signal (…) is by far subsidence in the Central Valley of California, which is fully saturated on the negative end of the color scale", but seem legitimately reluctant to quantify rates.

In the Western Alps and Italy, Serpelloni et al. (2013) interpolated their compilation of GPS data (Fig. 6a), following the *surface* spline interpolator of the *GMT* distribution (Wessel et al., 2013). We carried out TR based on the same database, which is given in IGS realization of the ITRF2008. At long wavelengths, their interpolated map is similar to that obtained from TR (Fig. 6b). Typically, both studies suggest that rates vary quickly from the fast uplifting Western Alps to the quickly subsiding Po Plain. However, spline interpolation yields a rough surface, with rates varying quickly laterally, a pattern that is not reproduced by TR (Fig. 6b). This leads to local mismatches between the two maps that can exceed the mean absolute rates by an order of magnitude (Fig. 6c). This misfit is due to the tension assigned to the spline function in Serpelloni et al. (2013). Tension is hardly constrained on a physical basis, and therefore the misfit suggests that the data may not support the resolution that is proposed from a spline interpolation. The Western Alps are a noteworthy case, where uplift rates higher than 2 mm/yr or more have drawn attention (Serpelloni et al., 2013; Nocquet et al., 2016). As in the case of the Central Valley of California, TR suggests that observations may not entirely support such a signal. Importantly, our model is conservative, in the sense that it efficiently dampens the effect of outliers, within uncertainties; TR is capable to predict sharp contrasts (see the above California example) but naturally produces smooth interpolations when no data imposes otherwise. Furthermore, it is worth noting that the posterior level of scaling for data errors indicates that σ is higher than 2.5. However, this indicates that, contrary to the California/Nevada case, our level of fit is here much lower than the errors estimated by Serpelloni et al. (2013). Therefore, our analysis does not rule out the possibility that the Western Alps are uplifting at a fast rate, but only suggests that more robust data is needed.

Some conclusions can be drawn from the comparisons of the three different methods, applied to two regions of North America and Europe. All three methods yield comparable results at first order, qualitatively. But they also differ by many aspects. TR and GPS Imaging both reproduce short wavelengths and sharp gradients in the densely surveyed regions of Nevada and California. However, long wavelengths are not interpreted similarly and global trends differ, though moderately. At short wavelengths, the magnitudes can depart considerably. GPS Imaging seems to be less conservative than TR, and more easily permits high magnitudes to appear. Comparing spline interpolation and TR in Europe indicates that the latter likely over-interprets very short wavelengths, and perhaps neglects uncertainties.

An outcome of our analysis is the level of fit σ. Because this value is close to 1 for the California/Nevada case, it suggests that underestimated uncertainties in the input dataset cannot be incriminated. Conversely, in the Western Alps and Italy, σ suggests that uncertainties in the dataset are potentially underestimated, which likely explains part of the difference in the results of the two methods. These contrasted behaviors thus point to the need to carefully select an appropriate method, but also to the fundamental impact of uncertainties. In the following, our goal is to provide a single method to map VLM at a global scale, and we thus opt for TR.

3. Results

3.1. Vertical land motion at long-wavelength

To produce a global view of VLM, we first carried out TR for a range of regions, each of them being defined in order to comprehensively tesselate most emerged lands (see details Table 1, in Appendix). Given the uneven physiography and data distribution, there is no systematic method to define individual regions. We defined each region in order to secure a minimum overlap between adjacent regions of at least 10 degrees. This overlap is meant to prevent edge effects and to optimize collating (i.e., *blending* with GMT, Wessel et al., 2013) individual maps into the global map shown in Fig. 7.

Not surprisingly, the most prominent feature is that of the fast uplifting high latitudes, where post-glacial rebound is the most visible. In the northern hemisphere, this is clearly the dominating signal in Fennoscandia, Greenland, the Hudson Bay, the Canadian Rocky Mountains, and at a lesser rate, Siberia. In the southern hemisphere, Antarctica is also uplifting, although at smaller rates than the northern counterpart. To an even lesser extent, Patagonia and South Africa are also uplifting. At mid latitudes and away from tectonically active

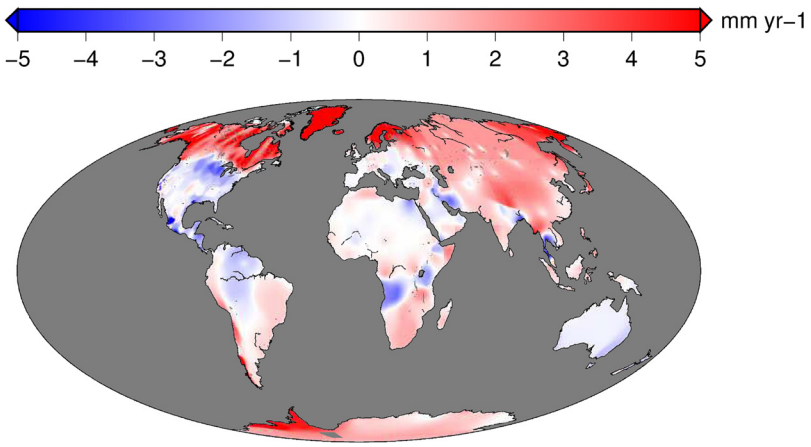

Fig. 7. *Observed* vertical land motion, as inferred from transdimensional regression of GPS data (mean value of the posterior distribution).

regions, continents mostly undergo modest VLM (absolute value lower than 1 mm/yr). This holds for South America, Africa, Australia, and North America (USA). Eurasia uplifts at a faster rate, which increases toward Siberia.

Within tectonically active zones, several active convergent systems display a specific VLM pattern that mirrors large-scale geodynamics. In view of the time frame considered, of its large scale, and since MIDAS filters out discontinuities, the reconstructed VLM should in principle not be related to the seismic cycle. However, the post-seismic deformation that follows megathrust earthquakes occasionally lasts for several years, and short time series may be affected by such events. Moreover, because areas that undergo post-seismic deformation in the aftermath of giant earthquakes can be large, it can affect multiple stations that nevertheless show robust trends. In such unfortunate case, a component of post-seismic deformation may occasionally contaminate the longterm, inter-seismic VLM that the TR method attempts to image. In such case, our method is expected to yield hybrid rates between post-seismic and inter-seismic deformation.

VLM at plate boundaries is remarkably imaged along the west coast of South America, where subduction related uplift prevails all along the Andes from Columbia to Patagonia (Fig. 7). It suggests that the Andes are continuously rising at a rate that varies along-strike from less than 1 mm/yr in Ecuador to more than 5 mm/yr in Patagonia. Some of this uplift is elastic due to the adjacent megathrust. In the Patagonian ice fields, a large part of the southernmost uplift is due to post-glacial rebound, which triggers peak uplift rates of up to 40 mm/yr at the location of the ice fields (Richter et al., 2016). Conversely, foreland basins on the eastern side of the Andes subside where sedimentation rates are the highest, from Venezuela to the north, to the south of Bolivia. Farther south, slow uplift prevails in Argentina and Chile; this hinterland pattern, away from the Andes, possibly mirrors transient dynamic topography above the Nazca (Dávila and Lithgow-Bertelloni, 2013; Flament et al., 2015) and Antarctica (Guillaume et al., 2009; Pedoja et al., 2011) subduction zones. Last, GIA is thought to contribute by up ~1.5 mm/yr in Patagonia (Zanchetta et al., 2014) (away from the ice-fields).

Along the Pacific subduction zones, subduction of the Farallon plate underneath the North American plate is now only active in the small margin of Cascadia, where the Juan de Fuca plate subducts. The interaction between neighboring plates is not mirrored by VLM, although the Western margin of North America is still actively deforming (e.g. Kreemer et al., 2014). In Alaska, uplift dominates at the plate margin, at a few mm/yr (Fig. 7). In the Aleutians and Kamtchatka, uplift occurs at a few mm/yr, which possibly manifests the deformation of the plate margin (Pflanz et al., 2013). Japan is densely covered by GPS stations. TR-imaged uplift there gradually decreases latitudinally from a mean rate of 2–3 mm/yr in Hokkaido, to 1–2 mm/yr in the north of Honshu, whereas the south of the archipelago is either stable or moderately subsiding. Of course, Japan is exposed to long-lasting post-seismic deformation following the 2011 Tohoku earthquake, which perturbs MIDAS trend estimates. Farther south along the Pacific subduction zone, subsidence in New Zealand gradually decreases latitudinally from ~1 mm/yr in the north and ultimately turns into slow uplift in the south.

Finally, the Tethyan convergence zone, which runs from the Western Alps to Myanmar, reveals a complex pattern of uplift and subsidence. Yet, some zones display a clear signal. The most striking signal appears in the convergence zone between India and Eurasia, wherein the Himalaya and Ganges plain show a remarkably contrasted behavior, which consistently reveals the geodynamic framework. TR-inferred rock uplift in the Himalaya and Tibet occurs at a rate of 1–2 mm/yr while the foreland Ganges plain is subsiding at −1 to −2 mm/yr. The sharp boundary between the uplifting Himalaya and subsiding foreland clearly delineates the Main Frontal Thrust of the Himalayan belt. Exhumation (e.g. Bernet et al., 2006) explains most of the rock uplift in the Himalaya, while subsidence could owe its origin to the joint effects of sediment loading (Najman et al., 2010), ground water depletion (Rodell et al., 2009; Chen et al., 2014; Long et al., 2016), and transient dynamic topography (Husson et al., 2014). Farther west, the Persian Gulf and SW Zagros subside at 1–2 mm/yr. Subsidence rates vary laterally and overall mirror the variations in the thickness of the modern foreland basins (Pirouz et al., 2017). Maximum rates of subsidence are found close to the depocenter, which indicates that VLM clearly responds to the same geodynamic mechanisms that cause basin subsidence. Last, the Western Alps are uplifting, probably as a response to multiple causes (postglacial rebound, erosional unloading, dynamic topography, etc. (see for instance, Serpelloni et al., 2013, and Section 2.3).

Our TR method interpolates all 10,602 data trends and aligns with a *Defendit numerus* approach (as already discussed for GPS stations by Bevis et al., 2013). Instead, one could opt for a careful selection of individual time-series in order to extract the most robust trends, as it is the case for the *ALTIGAPS* database (Pfeffer and Allemand, 2016). The drawback of preferring quality to quantity is the sparsity of the database: ALTIGAPS only contains 885 data points. The median value of the absolute difference between ALTIGAPS values and our TR predicted map of VLM at the same locations (Fig. 7) is 1.1 mm/yr (mean value is 1.7 mm/yr, and standard deviation is 2.0 mm/yr). Such discrepancy either indicates that many stations from the ALTIGAPS data base are not regionally representative of the long wavelength deformation of the Earth, or that uncertainties in either one or both methods are large (median uncertainty in ALTIGAPS is 0.55 mm/yr). Similarly, the analysis of Santamaría-Gómez et al. (2017) or Ostanciaux et al. (2011) is compatible with our analysis, although such studies only partially

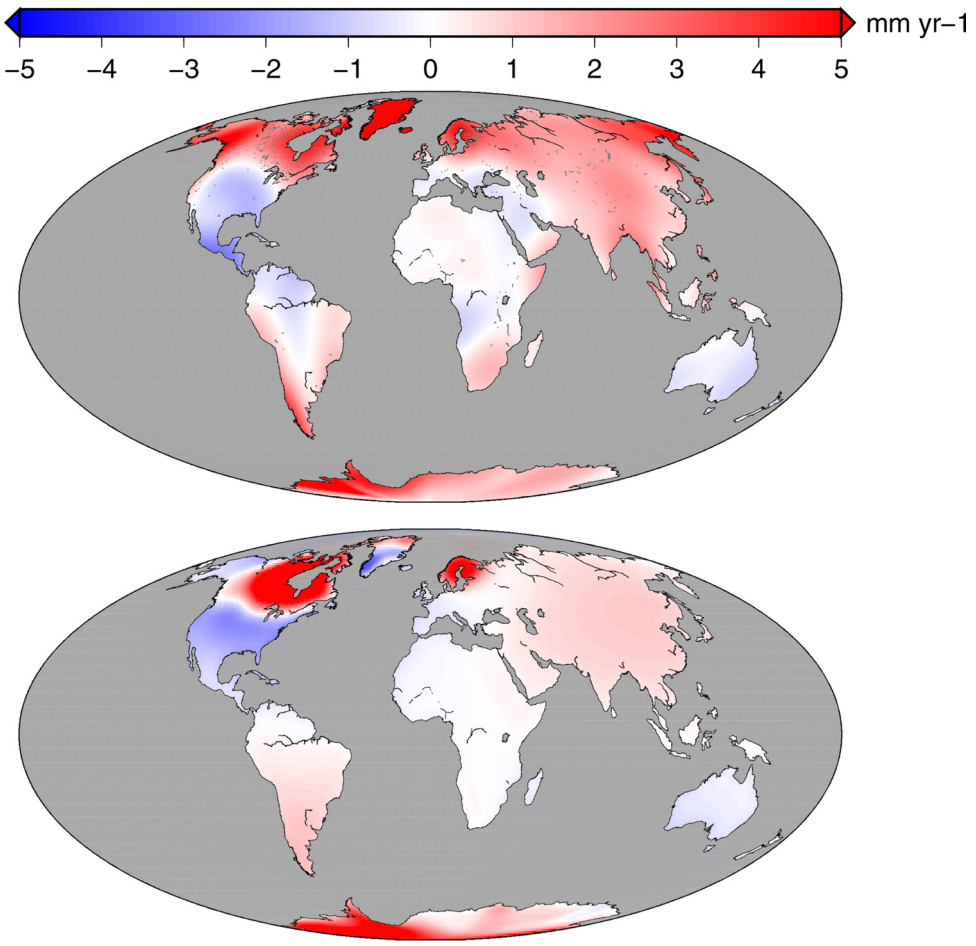

Fig. 8. (a) *Observed* vertical land motion, as inferred from transdimensional regression of GPS data (mean value of the posterior distribution, filtering out wavelengths shorter than 2500 km, Gaussian tapering between 5000 km and 2500 km). The digital version of the grid is available as online Supplementary Information. (b) *Predicted* vertical land motion from a forward numerical model of GIA (obtained solving SLE by the open source program SELEN (Spada and Stocchi, 2007), assuming the ICE-5G chronology and a three-layer volume average of the finely layered VM2 viscosity profile (Peltier, 2004).

provide means to critically appraise VLM at long wavelengths.

Last, Schumacher et al. (2018) very recently reappraised the collection of GPS time-series made available by NGL and applied a series of treatments in an attempt to rid trends from a variety of perturbations that contaminate the GIA signal, which includes the excluding of outliers and jumps (as in MIDAS release), subtracting a model predicted elastic response to the current melting of glaciers and ice-sheets and ocean loadings, and changes in the Earth's rotational pole relative to the 20th century average. The median value of the absolute difference between the refined database (~4000 selected datapoints) of Schumacher et al. (2018) and our TR predicted map of VLM at the same locations (Fig. 7) is 0.90 mm/yr (mean value is 1.14 mm/yr, and standard deviation is 1.12 mm/yr), yielding a closer adjustment than with ALTIGAPS.

3.2. Ground-truthing GIA predictions

In an attempt to map the VLM fingerprint of GIA, we filtered out wavelengths shorter than 2500 km (Fig. 8a; Gaussian tapering between 5000 km and 2500 km), in order to discard smaller-scale structures from our regression that could be due to crustal tectonics, water-pumping and other local features which are unlikely to relate to GIA. This allows for a comparison to the predictions from dynamic models. Of course, other processes than GIA also contaminate our filtered map. However, at such a long wavelength, we only expect dynamic topography to play a role (e.g. Pfeffer et al., 2017).

GIA can be modeled by solving the *Sea Level Equation (SLE)* first introduced by Farrell and Clark (1976), the integral equation governing the response of a spherically layered Earth model with viscoelastic rheology to surface loading (for a review, see Spada and Stocchi, 2006). The SLE has been recently generalized to account for horizontal migration of shorelines, for the growth and decay of marine-based ice, and for the effects of Earth rotation on sea level change (Mitrovica and Milne, 2003). In its simplest form, the SLE reads

$$S = N - U, \tag{1}$$

where S is the rate of variation of relative sea level at a given location, N is the rate of change of absolute (geocentric) sea level and U is the rate of vertical displacement of the solid surface of the Earth. N and U depend on the assumptions made about the melting chronology of the large continental ice sheets, and on the Earth's rheological profile, but since the SLE is implicit they shall also depend on S (Spada and Stocchi, 2006). The techniques presently adopted to solve SLE are described by, for instance, Spada (2017), to which the reader is referred for details. Here, we only mention that the fields U and N are retrieved from S once the SLE is solved; here we are not concerned with their time evolution since the LGM, but only with their values at present time. The GIA fingerprint for the rate of present-day uplift, shown in Fig. 8b, has been obtained solving the SLE from the open source program *SELEN* (Spada and Stocchi, 2007), assuming the ICE-5G chronology and a three-layer volume average of the finely layered VM2 viscosity profile (Peltier, 2004).

As a first test, we compare the spatial averages of the VLM field

obtained by TR and that obtained by forward models of GIA. In view of the uncertainties implied in the TR approach and inherent in the GIA modeling, a more rigorous comparison would probably be purposeless. We denote by U the present-day rate of vertical displacement associated with a given GIA model. Taking the average of SLE (see Eq. (1)) over the oceans (oc) provides

$$\langle S\rangle_{\mathrm{oc}} = \langle N\rangle_{\mathrm{oc}} - \langle U\rangle_{\mathrm{oc}}, \tag{2}$$

where S and N are the present-day rates of change of relative and absolute sea level, respectively, and the average is defined by $\langle f\rangle_{\mathrm{oc}} = A_{\mathrm{oc}}^{-1}\int_{\mathrm{oc}} f\,\mathrm{dA}$, where $f(\theta, \lambda)$ is any scalar field defined on the Earth's surface, θ and λ are colatitude and longitude, A_{oc} is the area of the oceans, and $dA = a^2 \sin\theta\, d\theta\, d\lambda$ is the element of area, a being Earth's radius.

We first note that the term $\langle N\rangle_{oc}$ represents the correction which is normally applied to satellite altimetry observations in order to remove the effects of GIA (e.g. Tamisiea, 2011). Of course $\langle N\rangle_{oc}$ shall depend on the particular GIA model chosen. Furthermore, assuming that the mass of the ice sheets is not currently subject to changes (this is the case for all the ICE-X models of W.R. Peltier) and that the surface of the oceans is constant as a first approximation, in Eq. (2) we have $\langle S\rangle_{oc} = 0$ (Spada, 2017). Accordingly we get

$$0 = n - \frac{1}{A_{\mathrm{oc}}}\int_{\mathrm{oc}} U\,\mathrm{dA}, \tag{3}$$

where we have defined $n = \langle N\rangle_{oc}$. Now, using $\int_{oc} + \int_{co} = \int_{ea}$, where subscripts oc, co and ea denote integrations over oceans, continents, and over the whole Earth's surface, respectively, and observing that $\int_{ea} U\,dA$ must vanish by the principle of mass conservation (Spada, 2017), from Eq. (3) we simply obtain the rule of thumb:

$$\langle U\rangle_{\mathrm{co}} = -\frac{A_{\mathrm{oc}}}{A_{\mathrm{co}}}n \approx -\frac{(7/10)A_{\mathrm{ea}}}{(3/10)A_{\mathrm{ea}}}n \approx -\frac{7}{3}n. \tag{4}$$

A plausible range for n has been obtained by Tamisiea (2011) from a grid search, varying the viscosity of the upper and lower mantle within broad intervals, but keeping fixed the melting chronology of the ice sheets to that of the GIA model ICE-5G(VM2): n falls within -0.15 and -0.45 mm/yr. Using an ensemble of 14 published GIA models, Huang et al. (2013) evaluated the possible range of variation of n, without allowing the rheological profiles to vary. The average value of n is -0.26 ± 0.14 mm/yr, where the uncertainty corresponds to two standard deviations (for the GIA model considered in Fig. 8b, n falls in the middle of this range, being $n = -0.26$ mm/yr). Hence, introducing the value of n proposed by Huang et al. (2013) in Eq. (4) gives the average rate of vertical uplift of the continents due to GIA

$$\langle U\rangle_{\mathrm{co}} = 0.61 \pm 0.32\,\mathrm{mm/yr} \quad (2\sigma), \tag{5}$$

This rate is consistent with the rate of vertical displacement effectively observed by TR, for which the mean value of the posterior distribution amounts to 0.64 mm/yr.

One can be concerned by the fact that the estimate of $\langle U\rangle_{co}$ given by Eq. (5) only accounts for the melting of Late Pleistocene ice sheets, and does not include the contribution from the present, rejuvenated melting of ice sheets. Assuming a uniform mass loss of 100 Gt/yr across the Greenland (GRE) and the Antarctic (ANT) ice sheets, and across glaciers and ice caps (GIC), Spada (2017) computed a low value for $\langle U\rangle_{oc}$, of the order of 0.01 mm/yr. This estimate is based on an elastic Earth model, since viscous effects are generally negligible on a decadal time scale. Mass conservation imposes $\langle U\rangle_{ea} = 0$; thus for each of the three sources $\langle U\rangle_{co} = -(7/3)\langle U\rangle_{oc}$. Further rescaling these values using the mass balances effectively assessed for GRE, ANT and GIC by the Intergovernmental Panel on Climate Change Fifth Assessment Report (Church et al., 2013) for the time period 1993–2010 (see Table 13.1 of the report), we find that for GRE, ANT and GIC, $\langle U\rangle_{co} \sim 0.20$ mm/yr. Since this is less than the uncertainty in Eq. (5), we can conclude that the contributions of present melting of ice sheets, glaciers and ice caps do not contribute significantly to the *average* uplift of continents. However, this may locally play an important role (Pfeffer et al., 2017).

This quantitative match encourages further comparison, and we now compare the two predictions more qualitatively. TR-derived VLM (Fig. 8a) and dynamic predictions of GIA uplift rate (Fig. 8b), are overall consistent in their long-wavelength patterns, for which amplitudes are also generally similar. Uplift is mostly predicted by both models (TR and SELEN) in Antarctica, in Fennoscandia, Canadian shield, Siberia and most of Eurasia (though at a faster rate in TR). Conversely, subsidence is conformably predicted in Australia, the southern part of North America (United States), and parts of Europe and Africa. Nevertheless, some differences persist. For instance, owing to their non-GIA origin, the Andean or the Himalayan cases are not returned by dynamic GIA predictions (Fig. 8b). But dynamic predictions of GIA and TR-inferred VLM also depart in other regions. The TR map (Fig. 8a) features variations at shorter wavelengths than dynamic GIA models. They may reveal large scale processes that are difficult to detect, like longterm variations of aquifers, permafrost, or dynamic topography, but uncertainties in dynamic GIA modeling – due to uncertainties in mantle rheology and in the past distribution of the ice sheets mass, and to the inaccurate constraints on ice dynamics – and to uncertainties in GPS time series – make difficult an objective interpretation.

Note that a quantitative way to compare results from our transdimensional regression and dynamic predictions could be achieved via a standard-score, i.e. by taking the difference between the mean value of the posterior and the dynamic predictions, normalized by the standard deviation of the posterior. Here, for simplicity, we opt for a qualitative comparison, which allows to extract prominent behaviors.

At shorter scales, many features are comparable too. For instance, Antarctica shows a remarkably similar pattern of uplift, which increases in the Antarctic peninsula, in both models. Conversely, Greenland shows the most dramatic contrast between TR and dynamic models; this is likely because on the one hand we have no GPS data reflecting bedrock motion in the middle of Greenland and on the other hand the observed VLM is strongly affected by rebound from present-day melting (Jiang et al., 2010; Bevis et al., 2012). In South America, observations indicate a long-wavelength subsidence pattern, while dynamic model predictions of GIA do not. This departure can be explained by transient dynamic topography (Dávila and Lithgow-Bertelloni, 2013; Flament et al., 2015) and sediment compaction. In both TR and dynamic models, uplift and subsidence are found in Africa, but maps do not overlap. Observations suggest that modest variations in uplift and subsidence occur at long-wavelengths, while dynamic model predictions indicate very minor uplift and subsidence.

3.3. Regional results: Europe and North America

Amongst the different maps, Europe and North America are particularly relevant, simply because they benefit from the longest time series, and with a denser coverage than in any other region (Fig. 1). These two regions are sufficiently covered that the resolution of TR estimates of uplift rates can be compared along the coastlines to the rates of relative sea level change that we previously inverted for, applying TR to tide gauges analysis results by Choblet et al. (2014).

In Europe (Fig. 9), Fennoscandia dominates the signal and outlines the postglacial rebound centered in the north of the Baltic Sea, at about 10 mm/yr. Note that Fennoscandia is the location of largest standard deviation, as also imaged by the probability density function (*pdf*) of VLM along chosen profiles (Fig. 10). Probability density functions are better visualised in 2D, where they fully reveal the predictive power of our method. We thus extracted pdfs along the coastlines of Europe (Fig. 10a) and along a N-S profile that runs from Fennoscandia to the Aegean (Fig. 10b). The pdfs reveal that the signal is well resolved everywhere in Europe. Fennoscandia uplifts at more than 5 mm/yr, and peaks to ~10 mm/yr in the north of the Gulf of Bothnia, which

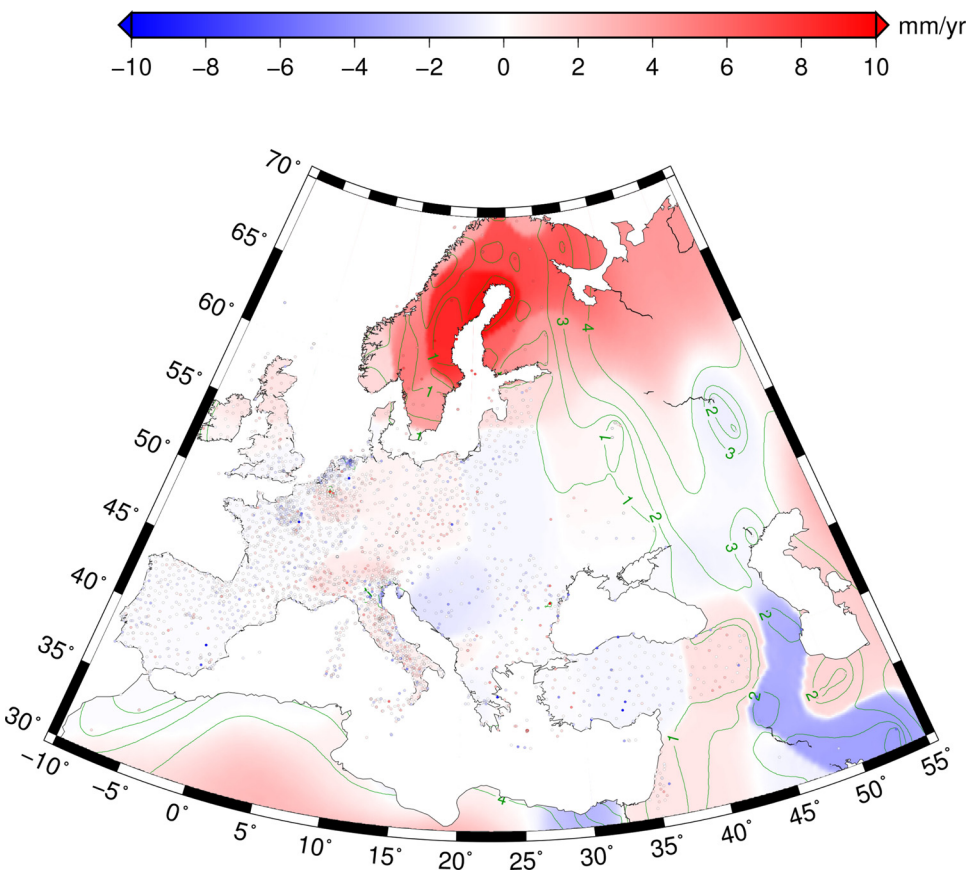

Fig. 9. *Observed* rate of vertical land motion, Europe, as inferred from transdimensional regression of GPS data (median value of the posterior distribution). The digital version of the complete posterior distribution is available as online Supplementary Information. Green curves outline the standard deviation of the posterior distribution (isocontours 1 mm/yr).

confirms independent estimates (e.g. Ekman, 1996; Steffen et al., 2009). The profile that runs along the coastline (Fig. 10a) features a broad pdf, a few mm/yr wide in the Baltic Sea. The relatively high uncertainty in Fennoscandia reveals the fact that the quality of the time series is lower than in more southern regions (although in principle MIDAS filters out periodic oscillations, climate – snow accumulation in particular – may alter the time-series), and that the lateral variations of VLM is high too. A plausible explanation is the complex pattern of oceans and continents (the Baltic Sea and surroundings in particular) that renders GIA more complex in Fennoscandia than elsewhere. Uncertainty nevertheless remains small with respect to the absolute value of VLM. The north-south trending pdf profile (Fig. 10b) shows similar results.

Western Europe, at latitudes lower than ~55° has an overall low

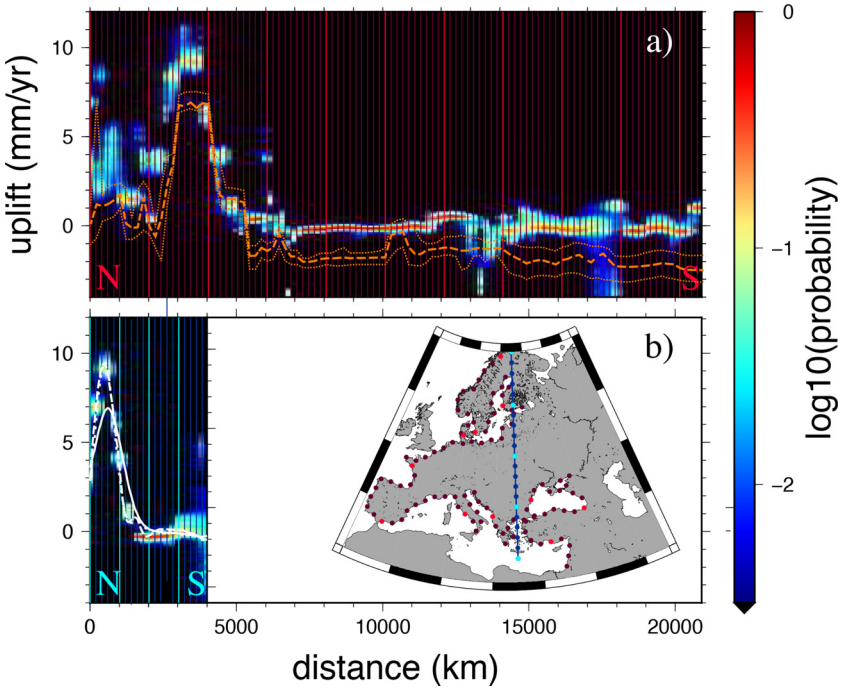

Fig. 10. Probability density function for the rate of vertical land motion in Europe. (a) Coastline, in red. Dashed orange curve shows relative sea level change, as interpolated from tide gauges (Choblet et al., 2014); rates of sea level change are multiplied by −1 in order to facilitate the comparison; the two dotted orange curves show the 95% credible interval; (b) north–south profile, in blue. Dark vertical lines every 200 km, lighter lines every 2000 km (a), and every 1000 km (b). Solid curve shows GIA predictions following the *SELEN* procedure of Spada and Stocchi (2007). Dashed and dotted curves are model predictions from Geruo et al. (2013) and Peltier et al. (2015). Inset shows the location of the profiles.

VLM (typically within the ± 0.5 mm/yr range). Fast uplift in the Western Alps has been debated over the last decade (Serpelloni et al., 2013; Nocquet et al., 2016) and some authors suggest that it could exceed 1 mm/yr and reach 2.5 mm/yr in part of the Western Alps. The origin of uplift remains unresolved (Nocquet et al., 2016); GIA is often considered, but model predictions (Stocchi et al., 2005; Norton and Hampel, 2010; Mey et al., 2016) are highly variable. In addition, our analysis suggests that direct observations may not robustly support such high rates either (see above). Again, our analysis only suggests that more robust data are needed before concluding that the Western Alps are uplifting at such a fast rate.

Anatolia shows a gradient from uplifting eastern Anatolia toward the slowly subsiding Aegean. This pattern could mirror the active mantle dynamics from underneath the plateau toward the subducting hellenic slab (e.g. Husson, 2006; Faccenna and Becker, 2010; Bartol and Govers, 2014; Ogretmen et al., 2018; Göğüş et al., 2017), but GIA contributes as well (Stocchi and Spada, 2007). The details of the eastern part of the region, including Persia and the Russian platform, are not well enough resolved to be confidently interpreted, as revealed by the standard deviation (Fig. 9) that exceeds the interpolated rates.

Comparing VLM to relative sea change provides information on absolute sea level change. Along European coastlines, VLM follows relative sea level change that we previously inferred following the same TR method (Fig. 10a, Choblet et al., 2014). The average value of the two curves are almost systematically offset by 2–3 mm/yr, in the range of estimates of absolute sea level change rate during the 20th century (Spada and Galassi, 2012; Cazenave et al., 2014; WCRP Global Sea Level Budget Group, 2018). This graphically expresses the fact that everywhere but in Fennoscandia VLM cannot help mitigating absolute sea level rise. VLM is often smaller than the rate of sea level rise, which is of course critical in low-lying coastlines, most emblematically in regions like the Netherlands.

In North America (Fig. 11), postglacial rebound dominates in Canada, as expected from the many dynamic model predictions of GIA since the seminal work of Farrell and Clark (1976), or as revealed from earlier (Sella et al., 2007) and recent (Kreemer et al., 2018) analysis of GPS data. Maximal uplift rates are predicted around the Hudson Bay, at ~14 mm/yr. Several second order features are noticeable. The fast uplifting northern region shows important lateral variations in uplift rates, that range between ~2 and ~15 mm/yr, and that are not predicted by dynamic models (see for instance Fig. 8b). These variations are possibly due to inadequate rendering of the history of ice caps since the Last Glacial Maximum. A broad E–W trending zone of subsidence lies at the latitude of the Great Lakes. This depression is due to the inward mantle flow from the peripheral regions of the formerly glaciated areas toward the uplifting deglaciated regions. The absolute values of both uplift rates – at high latitudes – and subsidence rates – at lower latitudes – decrease westward, which is plausible from a mechanical standpoint, provided GIA is the main cause of VLM. Most of the southern part of North America is subsiding, but shorter wavelengths regions of uplift reveal that other processes occur at a smaller than continent scale. Lambeck et al. (2017) suggest that it may reveal the existence of multi-domed ice sheets in North America. The Great Plains are either slightly uplifting or remaining stationary. Subsidence seems to be particularly reinforced along almost all coastlines in the Gulf of Mexico and East Coast. Water and hydrocarbon pumping can be incriminated to explain the extremely fast subsidence rates in Texas and Louisiana (> 5 mm/yr), when they add up to sediment compaction (for instance, Galveston subsides at ~5.9 mm/yr due to groundwater mining, e.g. Rhein et al., 2013). Similarly, along the southern East Coast, water extraction from the geological reservoirs noteworthy causes subsidence and threatens the low lying coastal regions (Karegar et al., 2016).

Probability density functions along the coastlines of North America (Fig. 12a and b) and along a N–S profile (Fig. 12c) reveal the extremely variable resolution of our TR. In the northern regions and around the Hudson Bay, VLM reveals a consistent mean rate of up to 12 mm/yr. However the variance is much larger in some cases than in the southern counterpart. This result only reveals the fact that densely populated areas have been more intensively monitored. Not surprisingly, uncertainties along the coastline of California are extremely small (Fig. 12b), as they are along the East Coast, from Florida to New England.

The comparison with our previous estimates of relative sea level change (Choblet et al., 2014) are at first sight not as satisfying for North America as they are for Europe. It possibly reveals the fact that both VLM (current study) and relative sea level rise (Choblet et al., 2014) are not fully resolved, in particular at high latitudes, where tide gauges are sparser. This is particularly true along the northernmost 4000 km that circumscribe the Hudson Bay (Fig. 12a), and along the Baja California

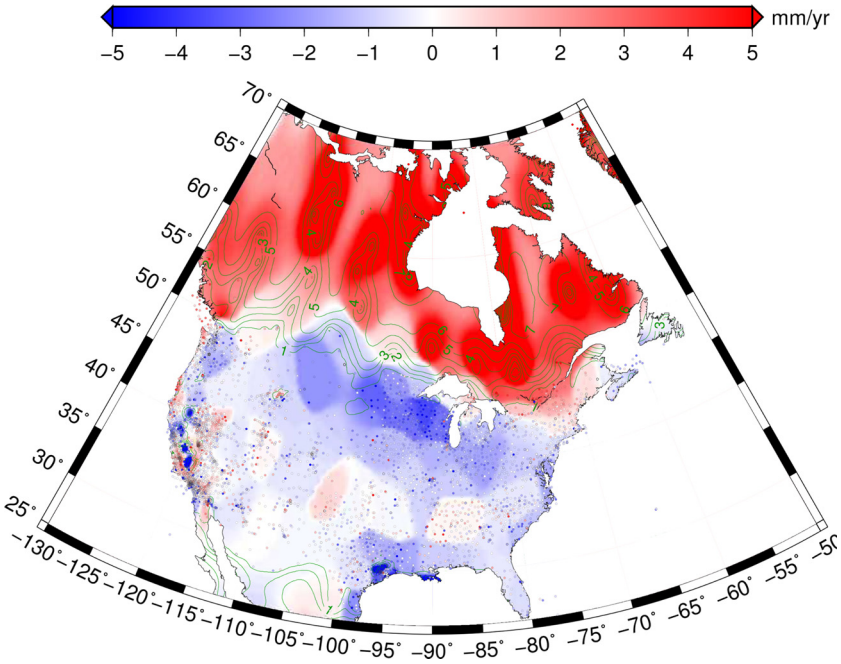

Fig. 11. *Observed* rate of vertical land motion, North America, as inferred from transdimensional regression of GPS data (median value of the posterior distribution). The digital version of the complete posterior distribution is available as online Supplementary Information. Green curves outline the standard deviation of the posterior distribution (isocontours 1 mm/yr).

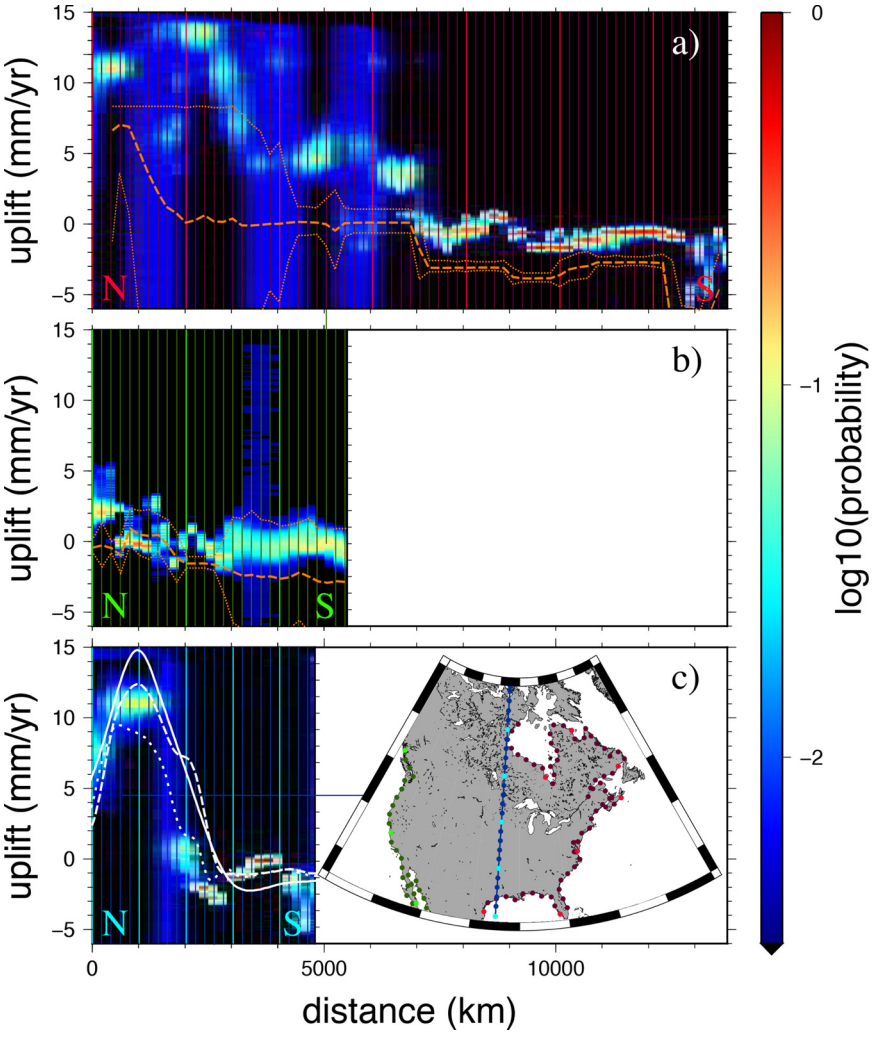

Fig. 12. Probability density function for the rate of vertical land motion in North America. (a) East Coast, in red; (b) West Coast, in green. Dashed orange curve shows relative sea level change, as interpolated from tide gauges (Choblet et al., 2014); rates of sea level change are multiplied by −1 in order to facilitate the comparison; the two dotted orange curves show the 95% credible interval, and (c) north–south profile, in blue. Dark vertical lines every 200 km, lighter lines every 2000 km (a and b), and every 1000 km (c). Solid curve shows GIA predictions following the *SELEN* procedure of Spada and Stocchi (2007). Dashed and dotted curves are model predictions from Geruo et al. (2013) and Peltier et al. (2015). Inset shows the location of the profiles.

and Gulf of California (Fig. 12b). In fact, uncertainties in the tide gauge record are very large. Along the East Coast, however, mean values vary accordingly and both uncertainties are small. Again, the comparisons of Fig. 12 along most of the East and West Coasts of North America, and certainly in the Gulf of Mexico, outline once more that VLM is either negative (subsiding), or too small to overcome the current rate of sea level rise, which remains an unescapable hazard.

Because pdfs provide a means to critically assess our predictions, they can be also compared to independently predicted values of GIA from dynamic models. Probing GIA predictions across the model shown in Fig. 7b, obtained using the program SELEN (Spada and Stocchi, 2007) yields a good fit (Fig. 10 and 12). For comparison, we also show model predictions of Geruo et al. (2013) and Peltier et al. (2015). All three models compare well to TR derived VLM. In Europe, the models of Geruo et al. (2013) and Peltier et al. (2015) ($ICE - 6G_C$ (VM5a)) are very similar. In Fennoscandia, our predictions are lower by ~2 mm/yr than both other models and TR derived uplift rates. Toward the south, uplift rates decay over ~1000 km while dynamic models decay over ~2000 km. A plausible explanation is that the rheological model does not allow for localized deformation, and therefore cannot account for fast changes in strain rates in the mantle.

In North America, models generally agree. Importantly, all three dynamic models as well as TR consistently predict, from North to South: high uplift rates within the polar circle that increase to reach peak values in the Hudson Bay, then quickly decreasing toward the United States to reach subsidence rates of ~ −2 mm/yr. Then, VLM reverses to become almost neutral in the Great Plains. Again, departure is maximal where uplift rates peak, at high latitudes: our TR model underestimates uplift rate predictions from our dynamic model (Fig. 8b) by ~3 mm/yr, and the model of Geruo et al. (2013) by ~1 mm/yr, while model predictions of Peltier et al. (2015) are too low by ~2 mm/yr. Our TR model predicts a decay of uplift rates over shorter distance (~1000 km) than dynamic models (~2000 km). Overall, unfiltered TR results tend to show sharper boundaries of the previously ice-covered regions than predicted by models. The transition distance is small and dynamic models do not reproduce such a sharp boundary between uplift and subsidence. This observation is compatible with the more local analysis of the tilt of Lake Michigan explored by van der Wal et al. (2009). Similarly to Europe, a plausible explanation is that the rheological structure of dynamics model does not allow for localized deformation. Finally to the south, fast subsidence in the Gulf of Mexico, which is unrelated to GIA, is not predicted by dynamic models.

4. Conclusions

Our analysis reveals first that the dataset that we use (trends of VLM on GPS time series) is mature in regions where the number of GPS time series is large enough. There, trends of VLM become relevant when analyzed jointly and examined from a probabilistic standpoint. Regions that have benefited from long time series and dense networks are appropriate to disentangle the different contributors of VLM. GIA dominates at long wavelength, and other processes like time variations of dynamic topography or large aquifers seemingly contaminate the signal only to a lesser extent. Shorter wavelength features reveal that other

sources like tectonics, sediment compaction, water and hydrocarbon extraction are equally visible and well rendered by TR even where gradients are sharp.

One important conclusion is that TR derived uplift rates are overall compatible with several independent information. Dynamic models of GIA are certainly imperfect, but nevertheless predict results that are in line with our observations, and it is satisfactory to see that the two classes of models (dynamic and TR) are mutually supportive. Therefore, we encourage the use of the TR derived map, as an alternative, or complementary to forward model predictions of GIA. We extracted the mean VLM on continents as a unifying metric to compare them. Results are very close (0.61 and 0.64 mm/yr, respectively), which is indicative of their overall consistency. The two classes of maps depart from one another where other processes overwhelm the signal, and in most places in Europe and North America, those secondary processes are known. Localized differences between the TR-VLM and GIA could also be due to the rebound associated with the recent melting of glaciers in North America and Europe. One premise of our study was that the long-wavelength, VLM was dominated by GIA, and that other contributions are either of shorter wavelengths or lower amplitudes. The good agreement between the two classes of models supports this hypothesis.

Important implications arise from this statement, because it indicates that our method provides a means to decipher GIA contributions from the rest of the signal. Conversely, it implies that our method provides a means to evaluate other contributions. This is fundamental because knowledge of GIA is necessary in many fields of geosciences, but also for policy makers, in particular when it comes to assessing risks of sea level rise on low lying coastal regions (e.g. Hallegatte et al., 2013). GIA corrections are often done on the basis of predictions from dynamic models, often ignoring the large uncertainties that such models convey. A good illustration of the impact it might have is the wavelength of decay from the fast uplifting high-latitudes toward the south in North America. Dynamic models predict that the decay occurs over a characteristic distance of ~2000 km, while TR *observations* more likely suggest that it occurs over only ~1000 km. We contend that, in this extremely well documented region, where TR predictions are well supported, this is likely due to the difficulty to account for appropriate rheologies, and that TR predictions are more reliable. Consequences might not be so important in the Great Plains of North America, but this also applies to the East Coast. If the transition occurs over shorter wavelengths than suggested by dynamic model predictions, attempts to decipher the processes of sea level change along the East Coast of North America (e.g. Kemp et al., 2011; Long et al., 2014; Love et al., 2016) need to be appraised accordingly.

Another set of data that we confronted our model with gives estimates of rates of relative sea level change. This metric indistinguishably accounts for absolute, or eustatic, sea level change. In places where the MIDAS dataset is best documented (Europe and North America), the mean values of the TR derived VLM is systematically offset by ~2–3 mm/yr, which gives an estimate of the contemporary rate of absolute sea level rise. This result, based on a continuous mapping of VLM, therefore partially dampens the results of Pfeffer and Allemand (2016) wherein they observe at discrete locations that VLM and sea level rise vary at a similar magnitude. However, to go beyond computing the plain difference between TR derived VLM and relative sea level change, more accurate values could be retrieved from a dual inversion of both datasets (from tide gauges and GPS) at once. This analysis is beyond our current scope and shall be the subject of a further study.

Acknowledgements

We are grateful to Enrico Serpelloni and Bill Hammond for kindly providing the digital values of their results. We thank the numerous individuals and organizations that make data from their GPS stations freely available to the scientific community. We are grateful to Holger Steffen and two anonymous reviewers. SELEN can be obtained by the Computational Infrastructure for Geodynamics (CIG, https://geodynamics.org/cig/software/selen/) or upon request to GS. NGL database of MIDAS-derived GPS rates can be retrieved from http://geodesy.unr.edu. TB is funded by the European Union Horizon 2020 research and innovation programme under Grant Agreement No. 716542. GS is funded by a FFABR (Finanziamento delle Attività Base di Ricerca) grant of MIUR (Ministero dell'Istruzione, dell'Università e della Ricerca). Part of the computations where performed on the CCIPL facilities in Nantes.

Appendix A

See Table 1.

Table 1
Parametrization for each regional inversion.

Region	# used data	Admissible range (mm/yr)	Region ($lon_{min}/lon_{max}/lat_{min}/lat_{max}$)
Antarctica	99	−1/+22	−180/180/−90/−50
Africa	1866	−4/+4	−20/52/−35/37
Alaska–Aleutians–Japan	2421	−5/15	128/232/30/72
Asia	1289	−10/16	45/145/−15/50
Australia	624	−7/12	100/190/−50/0
Central America	3828	−16/10	−120/−45/−2/33
Central Asia	220	−7/7	45/80/20/50
Europe	3100	−4/12	−10/55/30/70
Greenland	132	0/30	−70/−10/57/84
North America	4981	−10/+14	−130/−50/25/70
South America	391	−5/14	−85/−35/−55/15
Siberia	1001	−4/+8	45/170/40/77
[a]California/Nevada	2077	−8/8	−125/−114/32.5/42
[b]Alps/Italy	822	−4/+4	−15/39/28/60

[a] California/Nevada inversion are performed with an earlier version of MIDAS database (as in Hammond et al., 2016, for comparison) in Figs. 4 and 5.

[b] Alps/Italy inversion is performed using the database provided by Serpelloni et al. (2013).

Appendix A. Supplementary data

Supplementary data associated with this article can be found, in the online version, at https://doi.org/10.1016/j.jog.2018.10.002.

References

Amos, C.B., Audet, P., Hammond, W.C., Bürgmann, R., Johanson, I.A., Blewitt, G., 2014. Uplift and seismicity driven by groundwater depletion in central California. Nature 509.

Argus, D.F., Landerer, F.W., Wiese, D.N., Martens, H.R., Fu, Y., Famiglietti, J.S., Thomas, B.F., Farr, T.G., Moore, A.W., Watkins, M.M., 2017. Sustained water loss in California's mountain ranges during severe drought from 2012 to 2015 inferred from gps. J. Geophy. Res.: Solid Earth 122, 10559–10585. https://doi.org/10.1002/2017JB014424.

Argus, D.F., Peltier, W.R., Drummond, R., Moore, A.W., 2014. The Antarctica component of postglacial rebound model ICE-6G_C (VM5a) based on GPS positioning, exposure age dating of ice thicknesses, and relative sea level histories. Geophys. J. Int. 198, 537–563. https://doi.org/10.1093/gji/ggu140.

Aster, R.C., Borchers, B., Thurber, C.H., 2005. Parameter Estimation and Inverse Problems, first edition. Academic Press, Boston. https://doi.org/10.1016/B978-0-12-385048-5.00001-X.

Austermann, J., Mitrovica, J.X., Latychev, K., Milne, G.A., 2013. Barbados-based estimate of ice volume at Last Glacial Maximum affected by subducted plate. Nat. Geosci. 6, 553–557. https://doi.org/10.1038/ngeo1859.

Bartol, J., Govers, R., 2014. A single cause for uplift of the Central and Eastern Anatolian plateau? Tectonophysics 637, 116–136. https://doi.org/10.1016/j.tecto.2014.10.002.

Bernet, M., van der Beek, P., Pik, R., Huyghe, P., Mugnier, J.-L., Labrin, E., Szulc, A., 2006. Miocene to Recent exhumation of the central Himalaya determined from combined detrital zircon fission-track and U/Pb analysis of Siwalik sediments, western Nepal. Basin Res. 18, 393–412. https://doi.org/10.1111/j.1365-2117.2006.00303.x.

Bevis, M., Brown, A., Kendrick, E., 2013. Devising stable geometrical reference frames for use in geodetic studies of vertical crustal motion. J. Geod. 87, 311–321. https://doi.org/10.1007/s00190-012-0600-5.

Bevis, M., Wahr, J., Khan, S.A., Madsen, F.B., Brown, A., Willis, M., Kendrick, E., Knudsen, P., Box, J.E., van Dam, T., Caccamise, D.J., Johns, B., Nylen, T., Abbott, R., White, S., Miner, J., Forsberg, R., Zhou, H., Wang, J., Wilson, T., Bromwich, D., Francis, O., 2012. Bedrock displacements in greenland manifest ice mass variations, climate cycles and climate change. Proc. Natl. Acad. Sci. U. S. A. 109, 11944–11948.

Blewitt, G., Hammond, W.C., Kreemer, C., 2018. Harnessing the GPS data explosion for interdisciplinary science. EOS. https://doi.org/10.1029/2018ES005636.

Blewitt, G., Kreemer, C., Hammond, W.C., Gazeaux, J., 2016. MIDAS robust trend estimator for accurate GPS station velocities without step detection. J. Geophys. Res. (Solid Earth) 121, 2054–2068. https://doi.org/10.1002/2015JB012552.

Blewitt, G., Kreemer, C., Hammond, W.C., Goldfarb, J.M., 2013. Terrestrial reference frame NA12 for crustal deformation studies in North America. J. Geodyn. 72, 11–24. https://doi.org/10.1016/j.jog.2013.08.004.

Bodin, T., Salmon, M., Kennett, B.L.N., Sambridge, M., 2012. Probabilistic surface reconstruction from multiple data sets: an example for the Australian Moho. J. Geophys. Res. (Solid Earth) 117, B10307. https://doi.org/10.1029/2012JB009547.

Bouin, M.N., Wöppelmann, G., 2010. Land motion estimates from GPS at tide gauges: a geophysical evaluation. Geophys. J. Int. 180, 193–209. https://doi.org/10.1111/j.1365-246X.2009.04411.x.

Cazenave, A., Dieng, H.-B., Meyssignac, B., von Schuckmann, K., Decharme, B., Berthier, E., 2014. The rate of sea-level rise. Nat. Clim. Change 4, 358–361. https://doi.org/10.1038/nclimate2159.

Chen, J., Li, J., Zhang, Z., Ni, S., 2014. Long-term groundwater variations in Northwest India from satellite gravity measurements. Glob. Planet. Change 116, 130–138. https://doi.org/10.1016/j.gloplacha.2014.02.007.

Choblet, G., Husson, L., Bodin, T., 2014. Probabilistic surface reconstruction of coastal sea level rise during the twentieth century. J. Geophys. Res. (Solid Earth) 119, 9206–9236. https://doi.org/10.1002/2014JB011639.

Church, J.A., Clark, P.U., Cazenave, A., Gregory, J.M., Jevrejeva, S., Levermann, A., Merrifield, M.A., Milne, G.A., Nerem, R.S., Nunn, P.D., Payne, A.J., Pfeffer, W.T., Stammer, D., Unnikrishnan, A.S., 2013. Sea Level Change.

Dávila, F.M., Lithgow-Bertelloni, C., 2013. Dynamic topography in South America. J. S. Am. Earth Sci. 43, 127–144. https://doi.org/10.1016/j.jsames.2012.12.002.

Dettmer, J., Molnar, S., Steininger, G., Dosso, S.E., Cassidy, J.F., 2012. Trans-dimensional inversion of microtremor array dispersion data with hierarchical autoregressive error models. Geophys. J. Int. 188, 719–734. https://doi.org/10.1111/j.1365-246X.2011.05302.x.

Dietrich, R., Ivins, E., Casassa, G., Lange, H., Wendt, J., Fritsche, M., 2010. Rapid crustal uplift in Patagonia due to enhanced ice loss. Earth Planet. Sci. Lett. 289, 22–29.

Ekman, M., 1996. A consistent map of the postglacial uplift of Fennoscandia. Terra Nova 8, 158–165.

Faccenna, C., Becker, T.W., 2010. Shaping mobile belts by small-scale convection. Nature 465, 602–605. https://doi.org/10.1038/nature09064.

Farrell, W.E., Clark, J.A., 1976. On postglacial sea level. Geophys. J. R. Astron. Soc. 46, 647–667. https://doi.org/10.1111/j.1365-246X.1976.tb01252.x.

Faunt, C., Sneed, M., 2015. Water availability and subsidence in California's central valley. San Franc. Estuary Watershed Sci. 13, 1–8.

Flament, N., Gurnis, M., Müller, R.D., Bower, D.J., Husson, L., 2015. Influence of subduction history on South American topography. Earth Planet. Sci. Lett. 430, 9–18.

Fox, M., Bodin, T., Shuster, D.L., 2015. Abrupt changes in the rate of Andean Plateau uplift from reversible jump Markov Chain Monte Carlo inversion of river profiles. Geomorphology 238, 1–14.

Freymueller, J.T., Woodard, H., Cohen, S.C., Cross, R., Elliott, J., Larsen, C.F., Hreinsdóttir, S., Zweck, C., 2013. Active deformation processes in Alaska, based on 15 years of gps measurements. Active Tectonics and Seismic Potential of Alaska. American Geophysical Union (AGU), pp. 1–42. https://doi.org/10.1029/179GM02.

Geruo, A., Wahr, J., Zhong, S., 2013. Computations of the viscoelastic response of a 3-D compressible Earth to surface loading: an application to Glacial Isostatic Adjustment in Antarctica and Canada. Geophys. J. Int. 192, 557–572. https://doi.org/10.1093/gji/ggs030.

Geyer, C., Møller, J., 1994. Simulation procedures and likelihood inference for spatial point processes. Scand. J. Stat. 21, 359–373.

Giunchi, C., Spada, G., Sabadini, R., 1997. Lateral viscosity variations and post-glacial rebound: effects on present-day VLBI baseline deformations. GRL 24, 13–16. https://doi.org/10.1029/96GL03773.

Göğüş, O.H., Pysklywec, R.N., Şengör, A.M.C., Gün, E., 2017. Drip tectonics and the enigmatic uplift of the central anatolian plateau. Nat. Commun. 8, 1538. https://doi.org/10.1038/s41467-017-01611-3.

Green, P., 2003. Trans-dimensional Markov chain Monte Carlo. Highly Structured Stochastic Systems, vol. 27. pp. 179–198.

Green, P.J., 1995. Reversible jump Markov chain Monte Carlo computation and Bayesian model determination. Biometrika 82, 711–732. https://doi.org/10.1093/biomet/82.4.711.

Guillaume, B., Martinod, J., Husson, L., Roddaz, M., Riquelme, R., 2009. Neogene uplift of central eastern Patagonia: dynamic response to active spreading ridge subduction? Tectonics 28 doi: 10.1029/2008TC002324.

Hallegatte, S., Green, C., Nicholls, R.J., Corfee-Morlot, J., 2013. Future flood losses in major coastal cities. Nat. Clim. Change 3, 802–806. https://doi.org/10.1038/nclimate1979.

Hammond, W.C., Blewitt, G., Kreemer, C., 2016. GPS imaging of vertical land motion in California and Nevada: implications for Sierra Nevada uplift. J. Geophys. Res. (Solid Earth) 121, 7681–7703. https://doi.org/10.1002/2016JB013458.

Huang, Z., Guo, J.-Y., Shum, C.K., Wan, J., Duan, J., Fok, H.S., Kuo, C.-Y., 2013. On the accuracy of Glacial Isostatic Adjustment models for geodetic observations to estimate Arctic ocean sea-level change. Terrestrial 24. https://doaj.org/article/6e9269d15841410885a8e139ebaf72c7.

Husson, L., 2006. Dynamic topography above retreating subduction zones. Geology 34, 741. https://doi.org/10.1130/G22436.1.

Husson, L., Bernet, M., Guillot, S., Huyghe, P., Mugnier, J.-L., Replumaz, A., Robert, X., Van der Beek, P., 2014. Dynamic ups and downs of the Himalaya. Geology 42, 839–842. https://doi.org/10.1130/G36049.1.

Jiang, Y., Dixon, T.H., Wdowinski, S., 2010. Accelerating uplift in the North Atlantic region as an indicator of ice loss. Nat. Geosci. 3, 404–407. https://doi.org/10.1038/ngeo845.

Karegar, M.A., Dixon, T.H., Engelhart, S.E., 2016. Subsidence along the Atlantic Coast of North America: insights from GPS and late Holocene relative sea level data. Geophys. Res. Lett. 43, 3126–3133. https://doi.org/10.1002/2016GL068015.

Kemp, A.C., Horton, B.P., Donnelly, J.P., Mann, M.E., Vermeer, M., Rahmstorf, S., 2011. Climate related sea-level variations over the past two millennia. Proc. Natl. Acad. Sci. U. S. A. https://doi.org/10.1073/pnas.1015619108.

Kierulf, H.P., Steffen, H., Simpson, M.J.R., Lidberg, M., Wu, P., Wang, H., 2014. A GPS velocity field for Fennoscandia and a consistent comparison to glacial isostatic adjustment models. J. Geophys. Res. (Solid Earth) 119, 6613–6629. https://doi.org/10.1002/2013JB010889.

Kopp, R.E., Kemp, A.C., Bittermann, K., Horton, B.P., Donnelly, J.P., Gehrels, W.R., Hay, C.C., Mitrovica, J.X., Morrow, E.D., Rahmstorf, S., 2016. Temperature-driven global sea-level variability in the Common Era. Proc. Natl. Acad. Sci. U. S. A. 113, E1434–E1441. https://doi.org/10.1073/pnas.1517056113.

Kreemer, C., Blewitt, G., Klein, E.C., 2014. A geodetic plate motion and global strain rate model. Geochem. Geophys. Geosyst. 15, 3849–3889.

Kreemer, C., Hammond, W.C., Blewitt, G., 2018. A robust estimation of the 3-D intraplate deformation of the North American plate from GPS. J. Geophys. Res.: Solid Earth 123, 4388–4412. https://doi.org/10.1029/2017JB015257.

Lambeck, K., Purcell, A., Johnston, P., Nakada, M., Yokoyama, Y., 2003. Water-load definition in the glacio-hydro-isostatic sea-level equation. Quat. Sci. Rev. 22, 309–318.

Lambeck, K., Purcell, A., Zhao, S., 2017. The north American late Wisconsin ice sheet and mantle viscosity from glacial rebound analyses. Quat. Sci. Rev. 158, 172–210. https://doi.org/10.1016/j.quascirev.2016.11.033.

Lambeck, K., Rouby, H., Purcell, A., Sun, Y., Sambridge, M., 2014. Sea level and global ice volumes from the last glacial maximum to the holocene. Proc. Natl. Acad. Sci. U. S. A. 111.

Long, A.J., Barlow, N.L.M., Gehrels, W.R., Saher, M.H., Woodworth, P.L., Scaife, R.G., Brain, M.J., Cahill, N., 2014. Contrasting records of sea-level change in the eastern and western North Atlantic during the last 300 years. Earth Planet. Sci. Lett. 388, 110–122. https://doi.org/10.1016/j.epsl.2013.11.012.

Long, D., Chen, X., Scanlon, B.R., Wada, Y., Hong, Y., Singh, V.P., Chen, Y., Wang, C., Han, Z., Yang, W., 2016. Have grace satellites overestimated groundwater depletion in the northwest India aquifer? Sci. Rep. 6 24398 EP.
Love, R., Milne, G.A., Tarasov, L., Engelhart, S.E., Hijma, M.P., Latychev, K., Horton, B.P., Törnqvist, T.E., 2016. The contribution of glacial isostatic adjustment to projections of sea-level change along the Atlantic and Gulf coasts of North America. Earth's Future 4, 440–464. https://doi.org/10.1002/2016EF000363.
Malinverno, A., Briggs, V.A., 2004. Expanded uncertainty quantification in inverse problems: hierarchical Bayes and empirical Bayes. Geophysics 69, 1005. https://doi.org/10.1190/1.1778243.
Malinverno, A., Parker, R.L., 2006. Two ways to quantify uncertainty in geophysical inverse problems. Geophysics 71, W15. https://doi.org/10.1190/1.2194516.
Mey, J., Scherler, D., Wickert, A.D., Egholm, D.L., Tesauro, M., Schildgen, T.F., Strecker, M.R., 2016. Glacial isostatic uplift of the European alps. Nat. Commun. 7.
Mitrovica, J., Milne, G., 2003. On post-glacial sea level: I. General theory. Geophys. J. Int. 154, 253–267.
Najman, Y., Appel, E., Boudagher-Fadel, M., Bown, P., Carter, A., Garzanti, E., Godin, L., Han, J., Liebke, U., Oliver, G., Parrish, R., Vezzoli, G., 2010. Timing of India–Asia collision: geological, biostratigraphic, and palaeomagnetic constraints. J. Geophys. Res.: Solid Earth 115.
Nocquet, J.-M., Sue, C., Walpersdorf, A., Tran, T., Lenôtre, N., Vernant, P., Cushing, M., Jouanne, F., Masson, F., Baize, S., Chéry, J., van Der Beek, P.A., 2016. Present-day uplift of the western Alps. Sci. Rep. 6.
Norton, K.P., Hampel, A., 2010. Postglacial rebound promotes glacial re-advances – a case study from the European alps. Terra Nova 22, 297–302. https://doi.org/10.1111/j.1365-3121.2010.00946.x.
Ogretmen, N., Cipollari, P., Frezza, V., Faranda, C., Karanika, K., Gliozzi, E., Radeff, G., Cosentino, D., 2018. Evidence for 1.5 km of uplift of the Central Anatolian plateau's southern margin in the last 450 kyr and implications for its multiphased uplift history. Tectonics 37, 359–390. https://doi.org/10.1002/2017TC004805.2017TC004805.
Ostanciaux, m., Husson, L., Choblet, G., Robin, C., Pedoja, K., 2011. Present-day trends of vertical ground motion along the coast lines. Earth – Sci. Rev. 110, 74–92.
Pedoja, K., Regard, V., Husson, L., Martinod, J., Guillaume, B., Fucks, E., Iglesias, M., Weill, P., 2011. Uplift of quaternary shorelines in eastern Patagonia: Darwin revisited. Geomorphology 127, 121–142.
Peltier, W., 2004. Global glacial isostasy and the surface of the ice-age Earth: the ICE-5G (VM2) Model and GRACE. Annu. Rev. Earth Planet. Sci. 32, 111–149. https://doi.org/10.1146/annurev.earth.32.082503.144359.
Peltier, W., Argus, D., Drummond, R., 2015. Space geodesy constrains ice age terminal deglaciation: the global ICE-6G_C (VM5a) model. J. Geophys. Res.: Solid Earth 120, 450–487.
Pfeffer, J., Allemand, P., 2016. The key role of vertical land motions in coastal sea level variations: a global synthesis of multisatellite altimetry, tide gauge data and GPS measurements. Earth Planet. Sci. Lett. 439, 39–47. https://doi.org/10.1016/j.epsl.2016.01.027.
Pfeffer, J., Spada, G., Mémin, A., Boy, J.-P., Allemand, P., 2017. Decoding the origins of vertical land motions observed today at coasts. Geophys. J. Int. 210, 148–165. https://doi.org/10.1093/gji/ggx142.
Pflanz, D., Gaedicke, C., Freitag, R., Krbetschek, M., Tsukanov, N., Baranov, B., 2013. Neotectonics and recent uplift at Kamchatka and Aleutian arc junction, Kamchatka Cape area, NE Russia. Int. J. Earth Sci. 102, 903–916.
Pirouz, M., Avouac, J.-P., Gualandi, A., Hassanzadeh, J., Sternai, P., 2017. Flexural bending of the Zagros foreland basin. Geophys. J. Int. 210, 1659–1680.
Rebischung, P., Griffiths, J., Ray, J., Schmid, R., Collilieux, X., Garayt, B., 2012. IGS08: the IGS realization of ITRF2008. GPS Solut. 16, 483–494. https://doi.org/10.1007/s10291-011-0248-2.
Rhein, M., Rintoul, S., Aoki, S., Campos, E., Chambers, D., Feely, R., Gulev, S., Johnson, G., Josey, S., Kostianoy, A., Mauritzen, C., Roemmich, D., Talley, L., Wang, F., 2013. Observations: ocean. In: Stocker, T., Qin, D., Plattner, G.-K., Tignor, M., Allen, S., Boschung, J., Nauels, A., Xia, Y., Bex, V., Midgley, P. (Eds.), Climate Change 2013: The Physical Science Basis. Contribution of Working Group I to the Fifth Assessment Report of the Intergovernmental Panel on Climate Change. Cambridge Univ. Press, Cambridge, United Kingdom and New York, NY, USA.
Richter, A., Ivins, E., Lange, H., Mendoza, L., Schröder, L., Hormaechea, J., Casassa, G., Marderwald, E., Fritsche, M., Perdomo, R., Horwath, M., Dietrich, R., 2016. Crustal deformation across the Southern Patagonian Icefield observed by GNSS. Earth Planet. Sci. Lett. 452, 206–215.
Rodell, M., Velicogna, I., Famiglietti, J.S., 2009. Satellite-based estimates of groundwater depletion in India. Nature 460, 999–1002. https://doi.org/10.1038/nature08238.
Sabadini, R., Gasperini, P., 1989. Glacial isostasy and the interplay between upper and lower mantle lateral viscosity heterogeneities. Geophys. Res. Lett. 16, 429–432. https://doi.org/10.1029/GL016i005p00429.
Sambridge, M., Bodin, T., Gallagher, K., Tkalcic, H., 2012. Transdimensional inference in the geosciences. Philos. Trans. R. Soc. Lond. Ser. A 371, 20110547. https://doi.org/10.1098/rsta.2011.0547.
Santamaría-Gómez, A., Gravelle, M., Dangendorf, S., Marcos, M., Spada, G., Wöppelmann, G., 2017. Uncertainty of the 20th century sea-level rise due to vertical land motion errors. Earth Planet. Sci. Lett. 473, 24–32.
Schumacher, M., King, M.A., Rougier, J., Sha, Z., Khan, S.A., Bamber, J.L., 2018. A new global gps data set for testing and improving modelled gia uplift rates. Geophys. J. Int. 214, 2164–2176. https://doi.org/10.1093/gji/ggy235.
Sella, G.F., Stein, S., Dixon, T.H., Craymer, M., James, T.S., Mazzotti, S., Dokka, R.K., 2007. Observation of glacial isostatic adjustment in "stable" North America with GPS. Geophys. Res. Lett. 34.
Serpelloni, E., Faccenna, C., Spada, G., Dong, D., Williams, S.D.P., 2013. Vertical GPS ground motion rates in the Euro-Mediterranean region: new evidence of velocity gradients at different spatial scales along the Nubia-Eurasia plate boundary. J. Geophys. Res.: Solid Earth 118, 6003–6024.
Simon, K., Riva, R., Kleinherenbrink, M., Tangdamrongsub, N., 2017. A data-driven model for constraint of present-day glacial isostatic adjustment in North America. Earth Planet. Sci. Lett. 474, 322–333 doi:10.1016/j.epsl.2017.06.046.
Smith, W.H.F., Wessel, P., 1990. Gridding with continuous curvature splines in tension. Geophysics 55, 293–305.
Spada, G., 2017. Glacial Isostatic Adjustment and contemporary sea level rise: an overview. Surv. Geophys. 38, 153–185. https://doi.org/10.1007/s10712-016-9379-x.
Spada, G., Barletta, V.R., Klemann, V., Riva, R.E.M., Martinec, Z., Gasperini, P., Lund, B., Wolf, D., Vermeersen, L.L.A., King, M.A., 2011. A benchmark study for glacial isostatic adjustment codes. Geophys. J. Int. 185, 106–132.
Spada, G., Galassi, G., 2012. New estimates of secular sea level rise from tide gauge data and GIA modelling. Geophys. J. Int. 191, 1067–1094.
Spada, G., Ruggieri, G., Sørensen, L.S., Nielsen, K., Melini, D., Colleoni, F., 2012. Greenland uplift and regional sea level changes from ICESat observations and GIA modelling. Geophys. J. Int. 189, 1457–1474.
Spada, G., Stocchi, P., 2006. The Sea Level Equation, Theory and Numerical Examples. Aracne, Roma.
Spada, G., Stocchi, P., 2007. SELEN: a Fortran 90 program for solving the "sea-level equation". Comput. Geosci. 33, 538–562.
Steffen, H., Gitlein, O., Denker, H., Mueller, J., Timmen, L., 2009. Present rate of uplift in Fennoscandia from GRACE and absolute gravimetry. Tectonophysics 474, 69–77.
Stein, M.L., 1999. Interpolation of Spatial Data: Some Theory for Kriging. Springer Series in Statistics. Springer, New York.
Stocchi, P., Spada, G., 2007. Glacio and hydro-isostasy in the Mediterranean Sea: Clark's zones and role of remote ice sheets. Ann. Geophys. 50. https://doi.org/10.4401/ag-3054.
Stocchi, P., Spada, G., Cianetti, S., 2005. Isostatic rebound following the alpine deglaciation: impact on the sea level variations and vertical movements in the Mediterranean region. Geophys. J. Int. 162, 137–147.
Tamisiea, M.E., 2011. Ongoing glacial isostatic contributions to observations of sea level change. Geophys. J. Int. 186, 1036–1044. https://doi.org/10.1111/j.1365-246X.2011.05116.x.
Voronoi, G., 1908. Nouvelles applications des parametres continus a la theorie des formes quadratiques. J. Reine Angew. Math. 134, 198–287.
van der Wal, W., Braun, A., Wu, P., Sideris, M.G., 2009. Prediction of decadal slope changes in canada by glacial isostatic adjustment modelling this article is one of a series of papers published in this special issue on the theme geodesy. Can. J. Earth Sci. 46, 587–595.
WCRP Global Sea Level Budget Group, 2018. Global sea level budget 1993–present. Earth Syst. Sci. Data Discuss. 2018, 1–88. https://doi.org/10.5194/essd-2018-53.
Wessel, P., Smith, W.H.F., Scharroo, R., Luis, J., Wobbe, F., 2013. Generic Mapping Tools: improved version released. Eos, Trans. Am. Geophys. Union 94, 409–410. https://doi.org/10.1002/2013EO450001.
Whitehouse, P., 2009. Glacial isostatic adjustment and sea-level change. State of the Art Report. Svensk Kärnbränslehantering AB, Swedish Nuclear Fuel and Waste Management Co., Stockholm, pp. 105.
Whitehouse, P.L., 2018. Glacial Isostatic Adjustment modelling: historical perspectives, recent advances, and future directions. Earth Surf. Dyn. Discuss. 2018, 1–50. https://doi.org/10.5194/esurf-2018-6.
Wu, P., Peltier, W.R., 1982. Viscous gravitational relaxation. Geophys. J. R. Astron. Soc. 70, 435–485. https://doi.org/10.1111/j.1365-246X.1982.tb04976.x.
Zanchetta, G., Bini, M., Isola, I., Pappalardo, M., Ribolini, A., Consoloni, I., Boretto, G., Fucks, E., Ragaini, L., Terrasi, F., 2014. Middle- to late-Holocene relative sea-level changes at Puerto Deseado (Patagonia, Argentina). Holocene 24.